

# Turbulent transients of monodisperse and polydisperse distributions of water drops through unstable borders of cloudy environments

Mina Golshan<sup>a</sup>, Shahbozbek Abdunabiev<sup>a</sup>, Mattia Tomatis<sup>a</sup>, Federico Fraternale<sup>a,1</sup>, Marco Vanni<sup>a</sup>, Daniela Tordella<sup>a,\*</sup>

<sup>a</sup>*Dipartimento di Scienza Applicata e Tecnologia, Politecnico di Torino, 10129 Torino, Italy*

---

## Abstract

An open question in atmospheric physics is the formation of clouds and the associated unsteady processes of nucleation, condensation, evaporation, collision, and fragmentation of water droplets. These processes occur mainly in the completely turbulent background airflow peculiar to cloudy environments. Of particular interest are the cloud boundaries because of their high inhomogeneity and anisotropy that, together with the intrinsic unsteadiness of the overall physical process, lead the system away from ergodicity.

In the present study, we use direct numerical simulation to study the temporal evolution of a perturbation localized on the turbulent layer that typically separates a cloud from the surrounding clear air. Across this shearless layer, a turbulent kinetic energy gradient naturally forms. Here, a finite perturbation in the form of local initial temperature fluctuation is applied to simulate a hydrodynamic instability inside the turbulent background airflow. A numerical initial value problem for two diametrically opposite types of drop population distributions is then solved. Specifically, we consider a mono-disperse population of droplets of 15  $\mu\text{m}$  of radius and a poly-disperse distribution with radii in the range 0.6 – 30  $\mu\text{m}$ . For both distributions, it is observed that the evaporation and condensation have a dramatically different weight inside the homogeneous cloudy region and the interfacial anisotropic mixing region. The initial monodisperse and polydisperse populations' dynamics exhibit substantial differences that can be exploited to understand the interplay of evaporation, condensation, and droplet collision. It is observed that the dynamics of drop collisions are highly affected by the turbulence structure of the host region. The two populations show a common aspect during their energy decay transient. That is the increased probability of collisions in the interfacial layer that houses intense anisotropic velocity fluctuations. This layer, in fact, induces an enhanced

---

\*Corresponding Author

Email address: [daniela.tordella@polito.it](mailto:daniela.tordella@polito.it) (Daniela Tordella)

<sup>1</sup>Current Address: Center for Space Plasma and Aeronomics Research, University of Alabama in Huntsville, Huntsville 35805 (AL), USA.

differentiation on droplets kinetic energy and sizes. Simulations are carried out in a domain of  $0.512 \times 0.512 \times 1.024$  m. An initial supersaturation around 2% is set in the cloud side, with an initial dissipation rate of the turbulent kinetic energy around  $500 \text{ cm}^2/\text{s}^3$ . Both polydisperse and monodisperse initial particle distributions contain  $10^7$  droplets, matching an initial liquid water content of  $0.8 \text{ g/m}^3$ . A computational scheme is proposed to get an estimate of the turbulent collision kernel for geometric collisions used in the population balance equations. A preliminary discussion is presented on the structure of the two unsteady nonergodic collision kernels obtained inside the cloud interface region.

*Keywords:* Turbulent shearless layer, Cloud-clear air interaction, Inertial particles, Water droplets, DNS, Gravity effects, Collision kernel.

---

## 1. *Introduction*

Atmosphere clouds are fascinating systems that host a rich and complex physics not yet completely known. They are still one of the most significant uncertainty factors for more reliable weather and climate prognoses. Many different methods of investigation are used to understand the multiple physical phenomenologies that regulate the life of clouds. The methods are in a continuous phase of development all over the world, which gives the index of the liveliness of research in this area. Whether it is field studies, or laboratory studies, or studies conducted by means of numerical simulations on machines capable of hosting High-Performance Computing, at state of the art, studies can only focus on sections or subsections of the physics globally involved. One aspect not yet understood is the fact that inside clouds, the kinetic energy is larger than in the clear air outside. Clouds behave as energy traps. The energy can be developed by inner physical-chemical processes as latent heat release by water drops nucleation and condensation or by turbulent energy amplification induced by unstable density stratification. However, energy captured from acoustic-gravity waves propagating into clouds from below or above cloud layers, or from cosmic rays during their interaction with water drops, or from electromagnetic radiations from the Earth or from outside the atmosphere should be taken into account. However, the measure or introduction into a numerical simulation of all these facts is yet very difficult. For instance, the compressibility must be included in a numerical simulation to account for internal acoustic and gravity waves and baroclinicity effects, but efficient techniques to carry out simulation of cloud at the evanescent relevant values of the Mach number have not been developed yet.

Cloud dynamics and lifetime as a whole is tightly coupled to entrainment processes and subsequent turbulent mixing at their interface. Turbulent flows are excellent at mixing fluids over a wide range of length scales. However, there are scenarios where turbulence fails to mix a system. For example, in the case of multi-phase flows, as clouds are, turbulence can cause clustering among water droplets, where droplets segregate from the gas flow and gather.

Drops nucleate in clouds when gaseous water vapour condenses on a substrate into water. Usually, they have diameters of less than 30 microns and follow air streamlines. In any case, droplets interact with each other with a low probability of collision.

The range of scales involved in the dynamics of a turbulent cloud cannot be covered by fully resolved numerical simulations [Atkinson and Zhang \(1996\)](#). The complexity of the multiscale cloud dynamics becomes fully apparent at the cloud boundary where air, water vapour, and droplets and less humid air, usually named as clear air, interact in a situation where turbulence is highly intermittent and anisotropic. Direct numerical simulations (DNS), which resolve the turbulence down to the finest scales, can help to associate turbulence dynamics to a simplified cloud microphysics model that includes droplet formation, growth, and interaction. In particular, inside a system configuration considered as being able to model the turbulence at the edge of an atmospheric cloud, which is the shear-less or shear-free mixing layer – one of the simplest set-ups of inhomogeneous turbulence. This layer forms when two homogeneous and turbulent regions with different mean kinetic energies are brought together. This configuration has been studied in experiments starting with [Gilbert \(1980\)](#), [Veeravalli and Warhaft \(1989\)](#) as well as in DNS by [Knaepen et al. \(2004\)](#), [Briggs et al. \(1996\)](#) or [Tordella and Iovieno \(2006\)](#), [Tordella and Iovieno \(2011\)](#).

In past literature, most simulations of lukewarm clouds, on average, assumed static and homogeneous conditions. We are interested in simulating more realistic regimes of warm clouds that actually are systems that live in perpetual transitional situations. These time evolutions highly depend on the turbulent airflow hosting the cloud and transport phenomena taking place through the complex surfaces that bound the cloud concerning the clear air surrounding it.

In our simulation, cloud boundaries (called interfaces in the following) are modelled through the shear-less turbulent mixing matching two interacting flow regions - a small portion of cloud and an adjacent clear air portion of equivalent volume - at different turbulent intensity. An initial condition reproduces local mild unstable stratification in density and temperature. The droplets model includes evaporation, condensation, collision, and coalescence.

In the present study, we aim at investigating the effect of transient anisotropic and highly intermittent turbulence on two opposite populations of water droplets. We implement both a mono-disperse and a poly-disperse population of particles. For the collision model, unlike [Franklin \(2005\)](#) (phantom collision model), we used a geometrical collision model combined with condensation- evaporation growth-decay. The paper is organized as follows: Section 2 provides a general description of the physical model for cloud droplets and cloud turbulence and the methodology used for this study. Section 3 describes the statistical results concerning the drop size distribution temporal evolution. Section 4 presents a preliminary investigation on the feasibility of obtaining a turbulent collision kernel in nonergodic conditions from the numerical experiment. Conclusions and outlook follow in Section 5.

## 2. The physical system

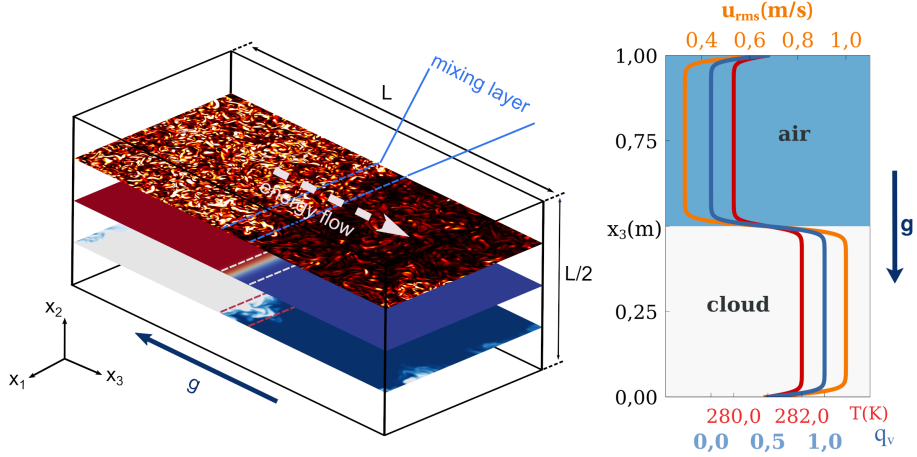
### 2.1. Turbulent air flow, temperature and water vapor mixing ratio fields

Our simulations focus on regimes of warm cumulus clouds, systems that live in transitional situations. Specifically, the cloud boundaries or interfaces are represented through a shear-less turbulent mixing in temporal decay. This flow is considered a good model for several reasons that link it to situations really present in nature, such as the intrinsic cloud non-stationarity, the ability to accommodate an integral scale gradient parallel to that of kinetic energy and enstrophy, the intrinsic anisotropy that includes the small, turbulent scales. In fact, it should be noticed, that the moment tensors of the derivatives of the speed fluctuations have main diagonals with different values of their terms ([Tordella and Iovieno \(2011\)](#)). The decaying shearless mixing is fundamental because it is straightforward since it is free of the turbulence production due to the presence of a mean shear, which is a situation relevant during most of the life of clouds. In fact, the presence of a mean shear is causing the dissolving of clouds. For the flow schematic, please, see Figure 1.

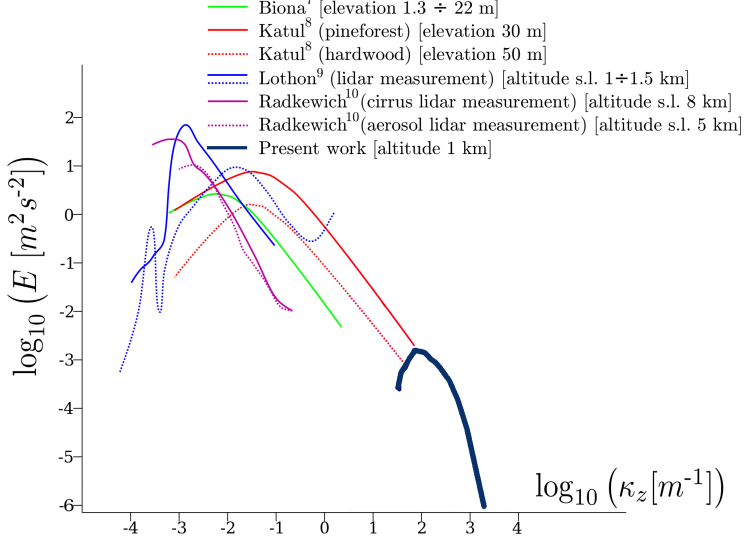
Shearless velocity fluctuation mixings are easily generated in 2D and 3D numerical simulations by exploiting periodical boundary conditions. In practice, they are produced by the interaction of two initially homogeneous isotropic turbulent flows (HIT) with different levels of (i) turbulent kinetic energy [Knaepen et al. \(2004\)](#), [Briggs et al. \(1996\)](#), [Tordella and Iovieno \(2006\)](#), [Tordella et al. \(2008\)](#), [Tordella and Iovieno \(2011\)](#), (ii) temperature [Iovieno et al. \(2014\)](#), [Kumar et al. \(2014\)](#), (iii) inertial particles [Ireland and Collins \(2012\)](#), also in the presence of supersaturation [Gotzfried et al. \(2017\)](#). This configuration has been studied also in laboratory experiments starting with [Gilbert \(1980\)](#) and [Veeravalli and Warhaft \(1989\)](#) where only mono-phase fluid turbulence was considered, to configurations where inertial particles were present [Good et al. \(2012\)](#), [Gerashchenko et al. \(2011\)](#).

The physical parameters of the simulations are set to match those of two interacting flow regions like those met at cloud borders. In such a mixing system, all transport processes are carried out by the fluctuations of the pressure and velocity fields. The governing equations are the incompressible Navier-Stokes equations, with the Boussinesq approximation for both temperature and vapour density, and active scalar transport equations for the water vapour and the thermal energy. The inertial cloud water drops are represented via a Lagrangian approach, including Stokes drag and gravitational settling. This representation is coupled to the vapor and temperature equations through their respective evaporation-condensation source terms. We follow the drop position, velocity, and radius. However, this is only a one-way coupling approach and does not include feedback from droplets to the fluid airflow field.

The size of the computational domain is  $0.5m \times 0.5m \times 1m$  and is discretized by using  $512 \times 512 \times 1024$  grid points. The Kolmogorov scale  $\eta_k$  is about 1 mm. Characteristic parameters of the turbulent flow fields are given in Table 1. A synthetic divergence-free field with a  $-1.67$  slope power spectrum in the inertial



(a) Schematics of the simulation domain (left panel) and of the initial profiles of the  $rms$  velocity (orange), temperature (red) and vapour content (blue) (right panel). The turbulent kinetic energy flow is from bottom to top along  $x_3$  direction,  $E_1/E_2 = 10$ .



(b) Three dimensional kinetic energy spectrum of the atmosphere turbulence observed in a set of infiel measurement campaigns. In blue, to the extreme right, the part of the spectrum relevant to the present simulations.

Figure 1: Overview of the physical system, cloud - clear air transient interaction, and of a few relevant averaged and spectral physical properties.

range and an exponential tail in the dissipation range (random phases) is used to build the initial condition for the velocity field. Specifically, after the generation

of the synthetic field, we let the high turbulent kinetic energy field (the cloud) evolve for few iterations until it reaches the dissipation of  $\epsilon \approx 500 \text{ cm}^2/\text{s}^3$ . A ratio of ten for the turbulent kinetic energy is set between the two regions, as well as different levels of temperature and supersaturation, see Table 1.

Model equations for the fluid flow are solved using the Fourier-Galerkin (FG) pseudo-spectral method as in [Iovieno et al. \(2001\)](#). The temporal integration uses a low storage second-order Runge-Kutta (RK2) method with exponential integration of the diffusive terms. The numerical code uses a one-dimensional slab parallelization and Message Passing Interface (MPI) libraries.

Similar to previous Direct Navier Stokes numerical simulation models, [Kumar et al. \(2014\)](#), [Gotzfried et al. \(2017\)](#), our code is neglecting compressible effects and is based on the incompressible Navier-Stokes equations under the Boussinesq approximation, where both the vapor mixing ratio field  $q_v(x_j, t)$ , which is given by the vapour density  $\rho_v$  referred to the dry air density, and the temperature  $T(x_j, t)$  are transported as passive scalars. The governing equations are given for the turbulent velocity field  $u_i(x_j, t)$ , the temperature field  $T(x_j, t)$ , the pressure field  $p(x_j, t)$  and the vapor mixing ratio  $q_v(x_j, t)$ . In the following, indices  $i, j, k$  are used within the Einstein convention.

$$\frac{\partial u_i}{\partial x_i} = 0 \quad (1)$$

$$\frac{\partial u_i}{\partial t} + u_j \frac{\partial u_i}{\partial x_j} = -\frac{1}{\rho_0} \frac{\partial p}{\partial x_i} + \nu \frac{\partial^2 u_i}{\partial x_j^2} - \mathcal{B} \delta_{zi}, \quad (2)$$

$$\frac{\partial T}{\partial t} + u_j \frac{\partial T}{\partial x_j} = \kappa \frac{\partial^2 T}{\partial x_j^2} + \frac{\mathcal{L}}{c_p} C_d \quad (3)$$

$$\frac{\partial q_v}{\partial t} + u_j \frac{\partial q_v}{\partial x_j} = \kappa_v \frac{\partial^2 q_v}{\partial x_j \partial x_j} - C_d \quad (4)$$

Here,  $\nu$  is the kinematic viscosity of air,  $g$  the gravitational acceleration,  $\rho_0$  is the reference value for the density of dry air,  $c_p$  the specific heat at constant pressure,  $\mathcal{L}$  the latent heat ( $2.48 \cdot 10^6 \text{ J kg}^{-1}$ ),  $k$  the temperature diffusivity,  $D$  the diffusivity of the vapor mixing ratio.  $C_d$  and  $\mathcal{B}$  are the condensation rate field and buoyancy field, respectively.

Upon the introduction of the volume average  $\langle \cdot \rangle$ , an average computed on the slice of domain normal to the vertical direction, i.e. the  $x_3$  direction, and thickness equal to the distance between two consecutive grid steps, the temperature fluctuations  $T'$  are given by

$$T'(x_j, t) = T(x_j, t) - \langle T(x_3, t) \rangle \quad (5)$$

where the volume averaged temperature is actually constant in time and equal to the sum of the temperature  $T_0$ , the average over the entire domain, and a linear background negative variation which sets the unstable stratification, thus  $\langle T(x_3) \rangle = T_0 + Gx_3$ , see Table 1. The initial temperature field term  $T'$  depends only on the  $x_3$  coordinate and has an hyperbolic tangent representation. For details, see Section 2.3.

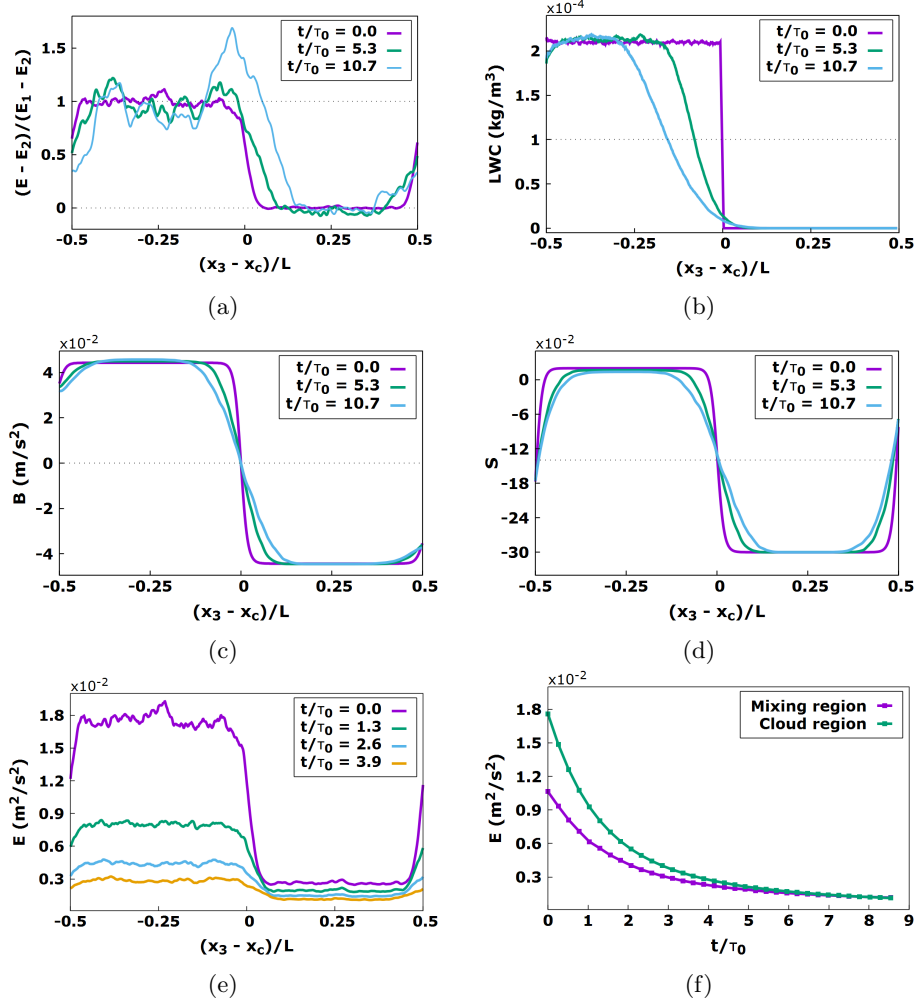


Figure 2: Kinetic energy, Liquid Water Content ( $LWC$ ), buoyancy and supersaturation mean values along the in-homogeneous direction at three stages along the temporal evolution that in physical non normalized terms last a few seconds ( $\tau_0 = 0.42$  s, see Table 2). The top left panel shows the turbulent energy excess with respect to the clear-air part, normalized with the difference difference between the two regions ( $E_1 = 10 \cdot E_2$ ) at  $t = 0$ .

The vapor mixing ratio fluctuations are given by

$$q'_v(x_j, t) = q_v(x_j, t) - \langle q_v(t) \rangle \quad (6)$$

In this case, the volume average is time dependent.

The buoyancy field  $\mathcal{B}$  in the momentum equation (2) depends on the temperature field  $T(x_j, t)$  and the vapor mixing ratio field  $q_v(x_j, t)$  and is defined

as:

$$\mathcal{B} = g[T' / < T > + \alpha q'_v] \quad (7)$$

where  $\alpha = M_a/M_v - 1 = 0.608$  and  $M_a$  and  $M_v$  are the dry air and vapor molar masses, respectively, see [Saito and Gotoh \(2018\)](#).

In this model, droplets affect the evolution of the fluid motion through the condensation term  $C_d$  in [3](#) and [4](#). The condensation rate field  $C_d = C_d(x_i, t)$  is defined as time derivative of the mass of liquid water,  $m_l$ , contained inside each of the grid cells with volume  $\Delta^3$  which surrounds the grid point  $x_i$ , referred to the mass of dry air  $m_a$ , [Vaillancourt et al. \(2001, 2002\)](#). Since cloud droplets are advected by the turbulent flow,  $C_d$  must be determined in the Lagrangian frame of reference used for the liquid water mixing ratio, which is described below in sub-section 2.2. For the use in equations [3](#) and [4](#),  $C_d$  must be in turn rendered into the Eulerian frame of reference. The condensation rate field is determined as:

$$C_d(x_i, t) = \frac{1}{m_a} \frac{dm_l(x_i, t)}{dt} = \frac{4\pi\rho_l K_s}{\rho_0 \Delta^3} \sum_{j=1}^{N_\Delta} R_j(t) S(X_j(t), t) \quad (8)$$

where  $m_a$  and  $m_l$  are the air mass and liquid mass per grid cell,  $\rho_l$  is density of water,  $\rho_0$  is reference density of dry air,  $R_j(t)$  and  $X_j(t)$  are the radius and vector space coordinate of the  $j$ -th drop, respectively.  $N_\Delta$  represents the number of drops inside each grid cell,  $S$  is supersaturation described below, see equation [13](#), and  $K_s$  is a temperature and pressure dependent diffusion coefficient that includes the self-limiting effects of latent heat release. In literature, for typical warm cloud conditions where the characteristic heat flux due to latent heating from a small variation in the droplet temperature is of the same order of the heat flux due to thermal conduction for the same temperature difference, this diffusion coefficient is considered to be constant because its temperature dependence is weak ( $K_s$  value in  $\text{m}^2 \text{ s}^{-1}$  ranges from  $5.07 \cdot 10^{-11}$  at  $T = 270 \text{ K}$ , to  $1.17 \cdot 10^{-10}$  at  $T = 293 \text{ K}$ ), see for instance [Rogers and Yau \(1989\)](#), [Gotoh et al. \(2016\)](#) [Kumar et al. \(2014\)](#)). In agreement to our volume averaged initial temperature of  $281 \text{ K}$ , we used the value  $8.6 \cdot 10^{-11} \text{ m}^2 \text{ s}^{-1}$ . The interpolation of the Eulerian field values at grid positions to the position occupied by the water droplets inside the cell is done via second order Lagrange polynomials. An inverse procedure is then used for the calculation of the condensation rate, which is determined at a first step at each droplet position and then relocated to the closest among the eight grid vertices.

## 2.2. Lagrangian Droplet Dynamics

In our simulations, cloud droplets are assumed to be point particles. Therefore they are always smaller than the grid size. The liquid water component is modelled as a Lagrangian ensemble of  $N$  point-like droplets. We consider two

different initial size distributions: a mono-disperse initial distribution of particles of size equal to  $15\mu\text{m}$  and an initial multi-disperse distribution of droplets of radii from  $0.6\mu\text{m}$  to  $30\mu\text{m}$ . It should be noted, that similarly to what done for the condensation rate field, Eulerian flow field quantities have to be determined at the droplet position to numerically proceed with Lagrangian equations. In this concern, we must highlight that we adopt a simplified feedback on the flow by droplets. The direct effect of the liquid droplet drag on the velocity field is neglected in the buoyancy term in the momentum equation. The feedback is therefore indirect and is confined to the coupling of the temperature field with the velocity field and the vapour mixing ratio through the condensation rate. The rationale for this position relies on the smallness of the drop Stokes numbers (drop Reynolds number much less than 1) and liquid mass loading.

The Lagrangian evolution for the  $i$ -th cloud droplet are given by

$$\frac{d\mathbf{X}_i}{dt} = \mathbf{v}_{p_i} \quad (9)$$

$$\frac{d\mathbf{v}_{p_i}}{dt} = \frac{\mathbf{u}(\mathbf{X}_i, t) - \mathbf{v}_{p_i}}{\tau_i} + \left(1 - \frac{\rho_a}{\rho_w}\right) \mathbf{g}, \quad (10)$$

where  $\mathbf{v}_{p_i}$  is the droplet velocity;  $\rho_w, \rho_a$ , are the densities of water and air, respectively;  $\mathbf{u}(\mathbf{x}_i, t)$  denotes flow velocity at the position of the  $i$ -th particle and  $\tau_i$  is the droplet response time. This time scale is defined by the Stokes drag coefficient and is adjusted to the droplet radius dynamical evolution,  $R_i = R(\mathbf{X}_i, t)$ . Therefore

$$\tau_i = \frac{2}{9} \frac{\rho_w}{\rho_a} \frac{R_i(\mathbf{X}_i, t)^2}{\nu}. \quad (11)$$

where  $\nu$  is the air kinematic viscosity. In this droplet model, we neglect a few other terms that can be of importance even when the Reynolds number is below unity. In particular, we neglect Faxen's correction associated to the velocity curvature effect on the drag, the added mass, the pressure gradient term and the Basset history force. In our simulation condition, where the gas and particle density ratio is of order  $10^{-3}$ , these forces are really negligible, as previously shown by many studies, see among others, [Armenio and Fiorotto \(2001\)](#), [Bergougnoux et al. \(2014\)](#).

In this investigation, the droplet growth is governed by three processes: condensation, evaporation and full coalescence after collision. Therefore, the numerical model for the growth of the particles must be coupled with the Lagrangian tracking of each droplet.

For what concerns the model of growth-by-condensation/evaporation, we reproduce a model for growth of particles according to the general dynamics described by the Kohler theory, which includes the spontaneous growth of cloud condensation nuclei (CCN) into cloud droplets under supersaturation water vapour conditions ([Kohler \(1936\)](#), [Howell \(1949\)](#) [Pruppacher and Klett \(1997\)](#), [Seinfeld and Pandis \(1998\)](#)). A simplified form of this model was also used by [Vaillancourt et al. \(2001\)](#), [Kumar et al. \(2014\)](#), [Gotoh et al. \(2016\)](#), [Gotzfried et al. \(2017\)](#) and [Gao et al. \(2018\)](#) for particles with size larger than CCN.

Fundamentally, as droplets are advected by the fluid where they can grow or evaporate in response to the local vapor field, the vapor mixing ratio is coupled to the droplet growth-decay through the supersaturation  $S$  which is defined in terms of the vapor mixing ratio and the saturation vapor mixing ratio as

$$S((\mathbf{X})_i, t) = \frac{q_v((\mathbf{X})_i, t)}{q_{vs}(T)} - 1. \quad (12)$$

The saturation vapor mixing ratio  $q_{vs}(T)$  at the droplet position is obtained from the Tetens formula ([Tetens \(1930\)](#)):

$$q_{vs}((\mathbf{X})_i, t) = \frac{e_s(T)}{R_v \rho_0 T} = \epsilon_0 \frac{610.78}{\rho_0 T} \exp[17.63 \frac{T - 272.16}{T - 35.86}] \quad (13)$$

where  $e_s$  is the saturation pressure, and  $\epsilon_0 = R_a/R_v \sim 0.62$  is the ratio between the gas constants for dry air and water vapor,  $R_a$  and  $R_v$ , respectively. For temperature above 273.16 K, see also [Monteith and Unsworth \(2008\)](#).

The curvature of the droplet surface induces the so called Kelvin effect on the evaporation rate. The bonding strength between water molecules lying on the droplet surface and its neighbors is lowered by the surface curvature. Therefore when the curvature is high, because the radii are small, the probability that water molecules may leave the liquid phase becomes higher. This increases the evaporation rate. Furthermore, the atmosphere is not clean since aside water droplets the atmosphere contains many other kinds of solid, or soft matter, or liquid, particles. Some of these are hydrophilic and water soluble. The effect of soluble CCN on the water evaporation rate is called the Raoult effect. The Kelvin and Raoult effects, the curvature and the solute effects, can be included in the model for the droplet growth. We follow [Hudson and Da \(1996\)](#) and [Ghan et al. \(2011\)](#) and [Saito and Gotoh \(2018\)](#) and write:

$$R_i \frac{dR_i}{dt} = K_s \left( S - \frac{A}{R_i} + \frac{Br_d^3}{R_i^3} \right) \quad (14)$$

Here, the diffusion coefficient  $K_s$  has been introduced above in relation to the condensation rate field  $C_d$ , see 8. The constant terms  $A$  and  $B$  represent the curvature (surface tension) and solute effects, respectively and  $r_d$  the dry particle radius. Term  $A$  directly depends on the surface tension of water ( $\sigma_w = 72.75 \cdot 10^{-7} [\text{J cm}^{-2}]$ ), and of course also on the density, the gas constant for water vapor and the local temperature of the air phase. While,  $B$ , aside the water and molecular weight of water, depends on the mass of solute, its molecular weight, and the total number of ions the solute molecule dissociates into. Here, we follow [Saito, Gotoh and Watanabe \(2019\)](#) and assume that the solute dissolved in each drop is an inorganic hygroscopic substance like ammonium sulfate, sulphuric acid or lithium chloride which have a solubility parameter  $B$  close to 0.7 and an accumulation mode with modal diameters  $r_d$  in the range from 10 to 50 nanometers (fine mode, observed North Atlantic marine air masses, see [Ovadnevaite et al. \(2017\)](#) and [Hudson and Da \(1996\)](#) and [Jensen and Charlson \(1984\)](#), [Flossman et al. \(1985\)](#)). For an air phase temperature nearly constant and close to 281 K we have  $A = 1.15 \cdot 10^{-7} \text{ cm}$  and  $B = 0.7 \cdot 10^{-18} \text{ cm}^3$ .

### 2.3. Initial and boundary conditions for the flow and scalar fields

The interaction between two homogeneous isotropic time decaying turbulence fields differing in only one property, the kinetic energy level, produces the simplest anisotropic turbulent flow. The simplicity of this flow lies mainly in the absence of the average velocity gradient, which means that there is no production of turbulent kinetic energy and no mean convective transport. All interaction is the result of the fluctuating pressure and velocity fields. In this investigation the two interacting flow fields are identical apart from the kinetic energy content, thus setting up a ratio (that is a gradient) of kinetic energy across the layer. Since it can be shown that the integral length scale of a turbulence field can be independent of its kinetic energy, it is possible to obtain, numerically, an inhomogeneity in the kinetic energy of two HIT fields while maintaining homogeneity in the length scale, [Batchelor \(1953\)](#).

The computational domain is a parallelepiped where periodic boundary conditions in all directions are imposed, see Figure 1, panel (a). In this nominally infinite domain the Navier-Stokes and passive scalar equations are solved with a fully dealiased (3/2 rule) Fourier-Galerkin pseudospectral method. Time integration is performed using a fourth order explicit Runge Kutta scheme. A parallelised version of the code for the velocity field is presented in [Iovieno et al. \(2001\)](#).

The initial conditions are generated by building a homogeneous isotropic velocity field within a volume  $2\pi \cdot 2\pi \cdot 2\pi$ , see [Wray \(1998\)](#). To create the initial condition, the velocity field is repeated creating a  $4\pi \cdot 2\pi \cdot 2\pi$  domain. In one side of the domain, each velocity component is multiplied by a constant, thus creating a ratio of energy between the fields, but keeping similar spectra and thus introducing no ratio of integral scales.

A hyperbolic tangent function is then used to smooth the interface and to define the initial mixing layer. This transition layer represents 1/40 of the  $4\pi$  domain. The matched field is

$$\mathbf{u}(\mathbf{x}) = \mathbf{u}_1(\mathbf{x})p(x_3) + \mathbf{u}_2(\mathbf{x})(1 - p(x_3)) \quad (15)$$

$$p(x_3) = \frac{1}{2} \left[ 1 + \tanh \left( a \frac{x_3}{L} \right) \tanh \left( a \frac{x_3 - L/2}{L} \right) \tanh \left( a \frac{x_3 - L}{L} \right) \right] \quad (16)$$

where the suffixes 1, 2 indicate high and low energy sides of the cloud interface model, respectively. Direction  $x_3$  is the in-homogeneous direction and  $L$  is the width of the computational domain in the  $x_3$  direction. Constant  $a$  in (16) determines the initial mixing layer thickness  $\Delta$ , conventionally defined as the distance between the points with normalized energy values 0.25 and 0.75 when the low energy side is mapped to zero and the high energy side to one. When  $a = 12\pi$  the initial ratio  $\Delta/L$  is about 0.026, a value that has been chosen so that the initial thickness is large enough to be resolved but small enough to have large regions of homogeneous turbulence during the simulations.

Tests were performed for domains of dimension  $4\pi \times (2\pi)^2$  with  $1024 \times 512 \times 512$  grid points and with an initial mixing layer representing 1/40 of the inhomogeneous dimension (largest grid dimensions in the mixing inhomogeneous direction).

The same technique is used to generate the periodical part  $T'$  of temperature field

$$T'(x_3, 0) = \Delta T \cdot \left[ \tanh\left(55\left(\frac{x_3}{L} - \frac{1}{2}\right)\right) - \frac{2x_3}{L} + 1 \right]$$

and of the water mixing ratio field, which are taken as non fluctuating fields at the initial time instant. See in Figure 1, right side of panel(a), a generic dimensional representation of the mean values of the temperature, water mixing ratio and root mean square of the air velocity. In this regards, see also Figure 2, where the average values along the inhomogeneous direction ( $x_3$ ) are shown at different stages along the temporal evolution.

In Figure 1, panel (b), we show the 3D kinetic energy spectra of the high energy homogeneous turbulent region of our system (dark blue line, ranging from  $k_3 = 25$  to  $k_3 = 1570$  [ $\text{m}^{-1}$ ]). This region represents the small portion of cloud interacting with the clear air lying on top of it. In the figure, this spectrum is compared with a few 3D spectra obtained by infield measurement campaigns carried out in the lower atmosphere. That is in the range from a few decades of meters (over pine and hardwood forests) to a few kilometers of altitude (cirrus and aerosol lidar measurements) and extending over Earth surfaces with linear dimension of the order of the atmospheric turbulence macroscale.

In Tables 1 and 2, the reader can find the parametrization used in the present Direct Numerical Simulations. The relevant physical and thermodynamics constants are gathered in Table 1, while domain specifications, computational grid structure, turbulence scales, field control parameters and water droplet population information are presented in Table 2.

Table 1: List of thermodynamics constants and flow field parameters and their corresponding values in the present DNS

Quantity	Symbol	Value	Unit
Latent heat of evaporation	$\mathcal{L}$	$2.48 \cdot 10^6$	$\text{J kg}^{-1}$
Heat capacity of the air at constant pressure	$c_p$	1005	$\text{J kg}^{-1} \text{K}^{-1}$
Gravitational acceleration	$g$	9.81	$\text{m/s}^2$
Gas constant for water vapour	$R_v$	461.5	$\text{J kg}^{-1} \text{K}$
Gas constant for air	$R_a$	286.7	$\text{J kg}^{-1} \text{K}$
Diffusivity of water vapour	$\kappa_v$	$2.52 \cdot 10^{-5}$	$\text{m}^2 \text{s}^{-1}$
Thermal conductivity of dry air	$\kappa$	$2.5 \cdot 10^{-2}$	$\text{J K}^{-1} \text{m}^{-1} \text{s}^{-1}$
Density of liquid water	$\rho_l$	1000	$\text{kg m}^3$
Dry air density, altitude 1000 m	$\rho_0$	1.11	$\text{kg m}^{-3}$
Reference kinematic viscosity	$\nu$	$1.399 \cdot 10^{-5}$	$\text{m}^2 \text{s}^{-1}$
Entire domain average temperature	$T_0$	281.16	K
Temperature in cloud region	$T_1$	282.16	K
Temperature in clear air region	$T_2$	280.16	K
Background temperature gradient	$G$	-2	$\text{K/m}$
Diffusion coefficient in eq.s 8 and 14	$K_s$	$8.6 \cdot 10^{-11}$	$\text{m}^2 \text{s}^{-1}$
Accumulation diameter	$r_d$	$0.01 \cdot 10^{-6}$	m
Kelvin droplet curvature constant	$A$	$1.15 \cdot 10^9$	m
Raoult solubility parameter for inorganic hygroscopic substances, like ammonium sulfate, lithium chloride, ...	$B$	0.7	-
Initial relative humidity inside cloud	$S$ (cloud)	1.02	-
Initial relative humidity inside clear air	$S$ (clear air)	0.7	-
Saturation vapor mixing ratio at $T_1$	$q_{vs}$ (cloud)	$0.79 \cdot 10^{-2}$	$\text{kg m}^{-3}$
Saturation vapor mixing ratio at $T_2$	$q_{vs}$ (clear air)	$0.69 \cdot 10^{-2}$	$\text{kg m}^{-3}$
Water saturation pressure at $T_0 = 281$	$e_s$	1.061	kPa
Molar mass of air	$m_{air}$	28.96	$\text{kg mol}^{-1}$
Molar mass of water	$m_v$	18	$\text{kg mol}^{-1}$
Initial liquid water content	$LWC$	$7.9 \cdot 10^{-4}$	$\text{kg/m}^3$

Table 2: List of parameters for the unstable cloud-clear interface direct numerical simulation hosting the monodisperse and polydisperse distribution of water droplets

Quantity	Symbol	Value	Unit
Simulation domain size	$L_{x_1} \cdot L_{x_2} \cdot L_{x_3}$	$0.512 \cdot 0.512 \cdot 1.024$	$\text{m}^3$
Simulation domain discretization	$N_1 \cdot N_2 \cdot N_3$	$512 \cdot 512 \cdot 1024$	
Simulation grid step	$\Delta x$	0.001	m
Kolmogorov time	$\tau_\eta$	$4.69 \cdot 10^{-2}$	s
Root mean square of velocity fluctuation in cloud region	$u_{rms}$	0.1125	$\text{m/s}$
Initial particle response time $R_0 = 15 \mu \text{m}$	$\tau_p$	3.2	s
Initial large eddy turn over time	$T_l = \tau$	0.42	s
Initial droplet radius for monodisperse distribution	$R_{in}$	15	$\mu\text{m}$
Minimum droplet radius for polydisperse distribution	$R_{in-p,min}$	0.6	$\mu\text{m}$
Maximum droplet radius for polydisperse distribution	$R_{in-p,max}$	30	$\mu\text{m}$
Total number of initial droplets (monodisperse population)	$N_{tot-m}$	$8 \cdot 10^6$	-
Total number of initial droplets (polydisperse population)	$N_{tot-p}$	$10^7$	-
Simulation time step	$\Delta t$	$9 \cdot 10^{-4}$	s
Initial energy ratio	$E_{cloud}/E_{clear air}$	10	-
Initial integral scale	$l$	0.048	m
Initial Taylor micro-scale Reynolds no.	$Re_\lambda$	42	-
Reynolds number based on domain dimension	$Re_L$	5000	-
Brunt-Väisälä amplification factor, where $N = (-g\Delta T T_0^{-1} L_{x_3}^{-1})^{0.5}$ , unstable stratification	$N^2$	-0.068	$\text{s}^{-2}$

## 2.4. *Monodisperse and polydisperse droplets initial distributions*

In this study we observe the two extremes between the possible population size distributions of water drops: a monodisperse versus a polydisperse population with uniform mass per class of radii. The two distributions tested in the present simulations are showed in figure 3.

As mentioned above, the two populations are evolving inside the inherently turbulent interfacial layer between the simulated small portion of the warm cloud and the clear air on top of it. The turbulent layer feels the unstable stratification (with a Brunt-Väisälä fluctuation growth factor  $N^2$  equal to  $-0.0687$ ) which corresponds to the velocity perturbation temporal amplification of  $0.26 \text{ s}^{-1}$  that was imposed at the initial instant and is followed by the free temporal decay. No forcing is set on the system which aims at modeling a realistic small cloud perturbation localized near the cloud boundary. It was in fact shown that the presence of a turbulence energy gradient is sufficient for Gaussian departure due to the anisotropy effects, and intermittency of velocity fluctuation and velocity derivative statistics, see Figures 6 - 8, 23. In fact, the turbulence energy gradient quickly leads the small scales of the turbulence out of isotropy and induces a pressure transport not negligible with respect to the turbulent velocity transport Tordella et al. (2008); Tordella and Iovieno (2011); Tordella and Iovieno (2012). All these aspects are active along with the transient evolution of the cloud/clear-air system and affect the drop collision rate in a way that has not yet been explored in literature so far. In particular, since in this situation the background airflow penetration inside the region of low turbulence is maximum, it is interesting to observe what happens to the droplet collision rate and penetration throughout the interfacial layer and into the clear-air portion of our system.

As for the types of distribution in size of the drops, the choice was motivated by the possibility of observing the dynamics associated to two different frequencies of the collisions. In fact, the monodisperse distribution, a drop size selected distribution, will present a small number of collisions given the fact that equal drops do not collide unless the local spatial variation of the turbulent air velocity are sufficient to give neighbouring drops different velocities leading to collision. See, for simplicity, the classical theories where turbulence is treated as steady, homogeneous and isotropic, with a small eddies length scale at least one order of magnitude larger than the drop size, East and Marshall (1954), Saffman and Turner (1955). The other way around, inside a polydisperse drop size distribution, the collision rate is high because different inertial drops show a different motion relative to the air and this is even more so because of gravity. On the other hand, it is recognized that the existence of a unique functional shape for the distribution size is still questioned on many grounds: different and competing mechanism for droplets nucleation, growth and removal are present in different context of cloud regions and cloud lives, see for instance the Chandrakar et al. (2020). Furthermore, with the aim to model a realistic cloud-clear-air boundary temporal evolution we are out of the ideal conditions, based on statistical steadiness in time and spatial homogeneity, that at the moment are the conditions that can lead to a theoretical treatment.

For instance, the recent approach based on the principle of maximum entropy (Liu and Hallett (1998) and Wu and McFarquhar (2018)) or the approach based on a Langevin equations representing the stochastic condensation-evaporation (McGraw and Liu (2006); Chandrakar et al. (2016); Siewert et al. (2017) and Saito et al. (2019)).

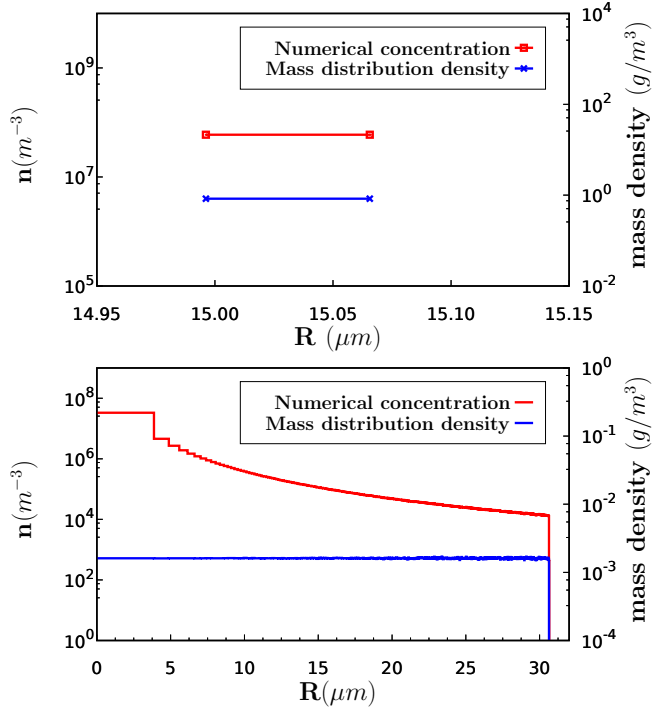


Figure 3: Monodisperse (top panel,  $8 \cdot 10^6$  particles) and Polydisperse (bottom panel,  $10^7$  particles) drop size distributions; for both distributions the initial value of total liquid content is  $LWC_0 = 0.8 g/cm^3$

### 3. Results

In the following, in a comparative way with respect to the two kinds of drop populations, we describe the results concerning the drop size growth (positive in case of condensation, negative in case of evaporation) and the modification of the distributions along the temporal transient which lasts around 10 eddy turn over times.

Inside both the volumes occupied by the cloud and the clear-air portions, we discuss the results of the computation of the drop collision time rate referred to the product of the numerical densities of collided droplets. This piece of information can be useful to understand, under our hypothesis of perfect collision-coalescence efficiency, the temporal evolution of the kernel of the aggregation integral term inside the Population Balance Equations. This term accounts for the formation of new particles resulting from the merging of two drops and has not yet determined under non ergodic conditions. The current attempt to evaluate the temporal evolution of kernel morphology aims to fill this gap and should be considered as a preliminary analysis required to understand how extensive the set of simulations must be to be sufficiently informative to allow an effective interpolation of kernel values. This is in order to build an approximate model representing a non-ergodic system evolution.

For three different transient stages, figure 4 shows the visualization of an inner slice of the computational domain normal to the interfacial layer where the water vapor, the velocity enstrophy and the droplet spatial distribution can be observed. A better view of the turbulence induced droplets dispersion across the interface can be seen in Figure 5.

#### 3.1. *Droplet size distribution temporal evolution. Condensation, evaporation, collision-coalescence.*

For a few time instants inside the transient, figures 9 and 10 show the numerical and mass concentrations for both drop populations. In both cases, it is evident a variation of the shape of the distribution inside the interaction layer.

In the monodisperse case, figure 9, the distribution progressively enlarges on the side of sizes smaller than the initial radius, which was 15  $\mu\text{m}$ . At about  $8.54\tau$ , inside the interaction zone, the numerical concentration of drops of 13  $\mu\text{m}$  is 100 times higher than in the cloud and the minimal radius is a bit lower than 11  $\mu\text{m}$ , while inside the cloud the minimal radius is slightly below 13  $\mu\text{m}$ . In the mixing layer, also much wider is the distribution width associated to collisions which involves coalesced droplet radii. It is noticeable that here collisions can happen between drops of radius different from the initial 15  $\mu\text{m}$ , e.g. between two drops slightly below radius 13  $\mu\text{m}$  or one drop of 11  $\mu\text{m}$  and another one of nearly 13  $\mu\text{m}$ , while inside the cloud portion collision happen almost only between droplets that both are close to 15  $\mu\text{m}$ , meaning that the evaporation is much more intense inside the anisotropic portion of the system. As can be quickly appreciated also by looking at panels c) and d) of figure 11, figure that describes the processes of condensation and evaporation concomitantly taking place in both parts of the system. We will come back to these aspects below.

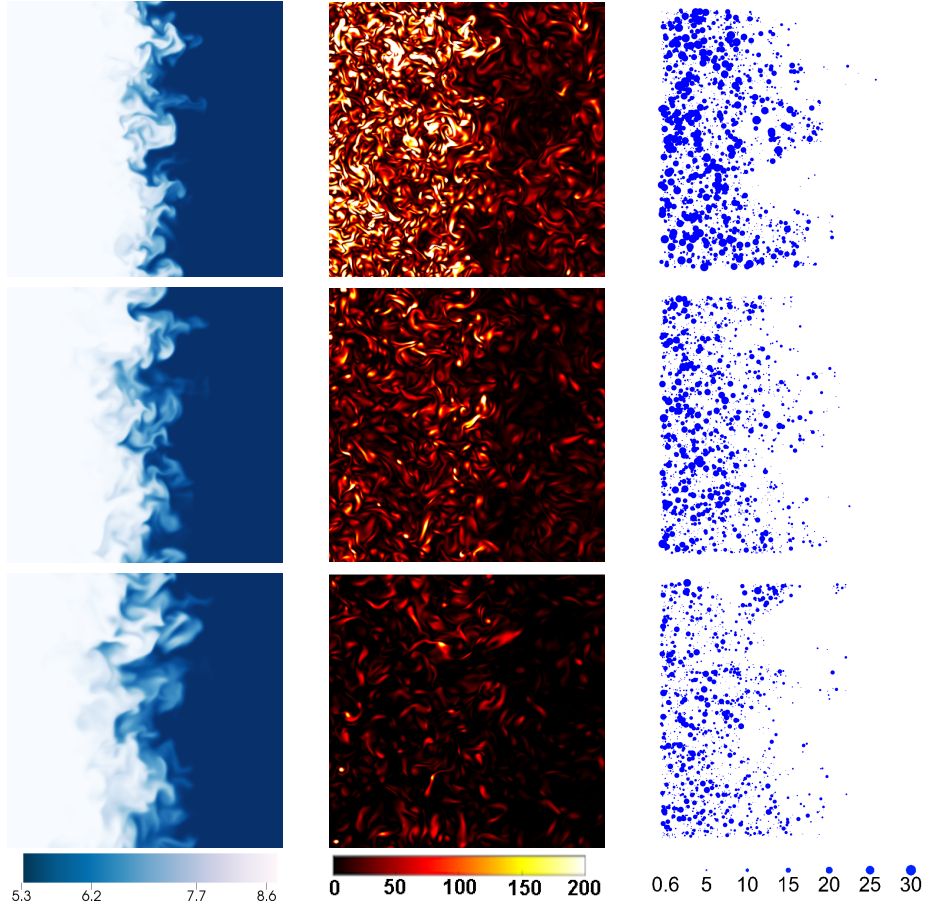


Figure 4: Visualization of the fields inside the shearless interface between the cloud portion and the clear-air portion of the simulation: water vapor (left, legend values in  $\text{kg}/\text{m}^3$ ), enstrophy (middle, values in  $\text{sec}^{-2}$ ) and droplets (right, diameters in arbitrary units). Snapshots at 3, 6 and 9 eddy turnover times.

Now, looking at the polydisperse distribution, which initially includes drops randomly positioned inside the cloud region with a mass uniform in the volume classes from 0.6 to 30  $\mu\text{m}$ , see figure 10, once again, we observe a more intense dynamics inside the interface region as compared to the cloud region. The numerical concentration highly differentiates in time inside the interface: for instance, for the larger radii, the ones close to 30  $\mu\text{m}$ , the decrease is of three order of magnitude, see panel b) of figure 10. Here, both in panels a) and b), one can appreciate the enlargement of the distribution up to radii around 38  $\mu\text{m}$ , the maximum radius reachable from the coalescence of two droplets of 30  $\mu\text{m}$ . However, in the cloud region, the growth by coalescence is accompanied by a robust condensation which is marginally present in the interface region beyond radii of 30  $\mu\text{m}$ , see panels a) and b) in figure 10.

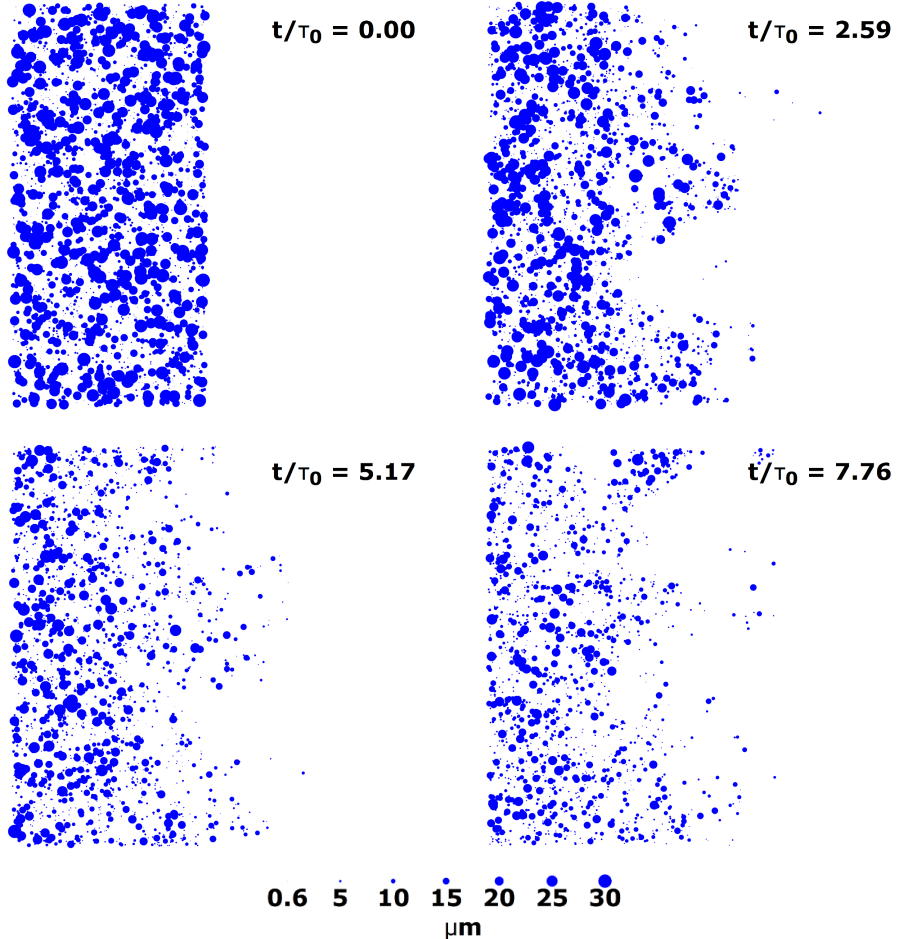


Figure 5: Visualization of the time varying water droplet distribution inside the cloud region and across the interface with the clear air ambient at a selected section parallel to the plane  $x_3, x_2$ . The section is  $\pi \times \pi$  wide in non dimensional terms. It can be appreciated that the concentration of the largest droplets is lowering due to the gravitational settling that displaces them out the visualized section.

Coming to figures 11, 12, we can discuss the different weight that condensation and evaporation have in the temporal evolution of the system. From top to bottom, these figures present data on the positive growth of the ray (condensation), on the negative growth (evaporation) and on their combined effects in a given instant near the end of the transient (8.0 parasitic rotation times).

Let us consider first, the mono-disperse population dynamics. In the left side of figure 11, one can see that inside the cloud portion the condensation action is present but milder than the evaporation, about 10 times less. Counter-

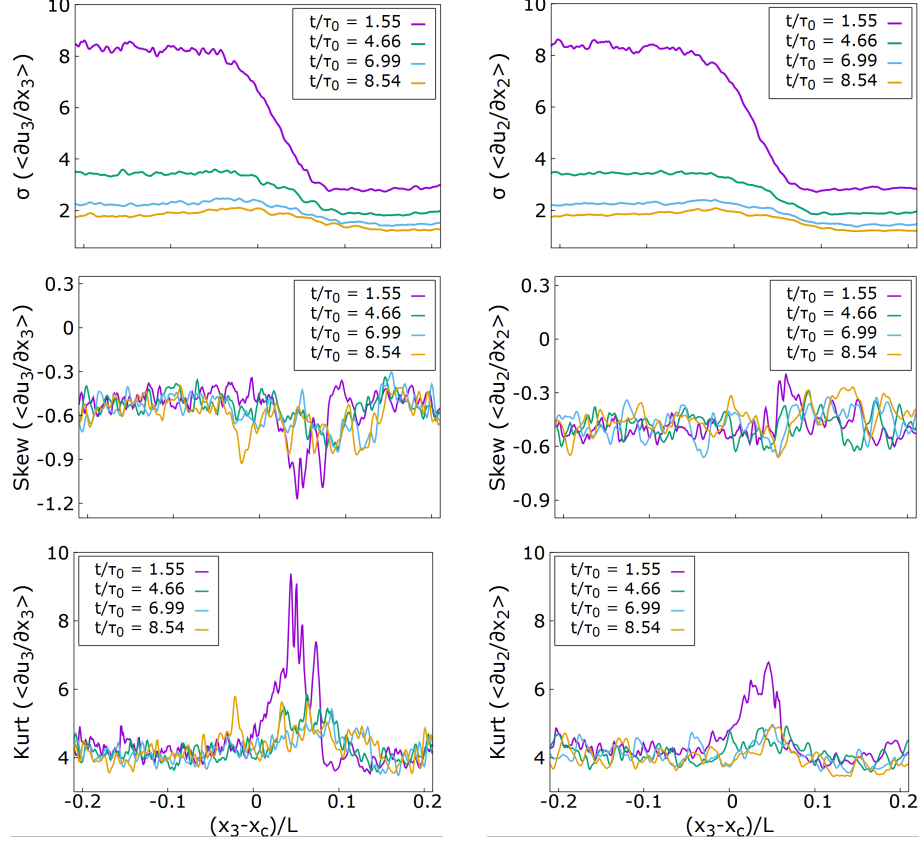


Figure 6: Statistical moments of the fluctuation of the velocity longitudinal  $x_3$  derivative. Left, derivative in the direction across the interface. Right, derivatives along the direction parallel to the interface. The different behaviour highlights the intrinsic anisotropy of the fine scales of the turbulence inside this shear free layer.

intuitively, condensation is proportionally more intense on collided-coalesced drops, see right side in panel a). Also counter-intuitively, we observe a small range of radii (13.5–13.7  $\mu\text{m}$ ) where condensation-evaporation balance perfectly, see panel c). Now, by considering the interaction region, panel b), d), f), we can observe an intense condensation for droplets close to 15  $\mu\text{m}$  and for the collided-coalesced droplets which gather around radii close 18.9  $\mu\text{m}$ . Evaporation is becoming in time very important and generates drops as small as 11.8  $\mu\text{m}$  after 8.54  $\tau_0$ , even if the kinetic energy inside the system is falling by 18 times in the cloud region and by 6 times in the clear-air region. Notice that inside the shearless interface layer, the evaporation is immediately active on collided particle, a thing which does not happen inside the cloud region. Overall, inside the interface region evaporation and collision prevail over condensation.

In the case of the polydisperse distribution, figure 12, the situation is dif-

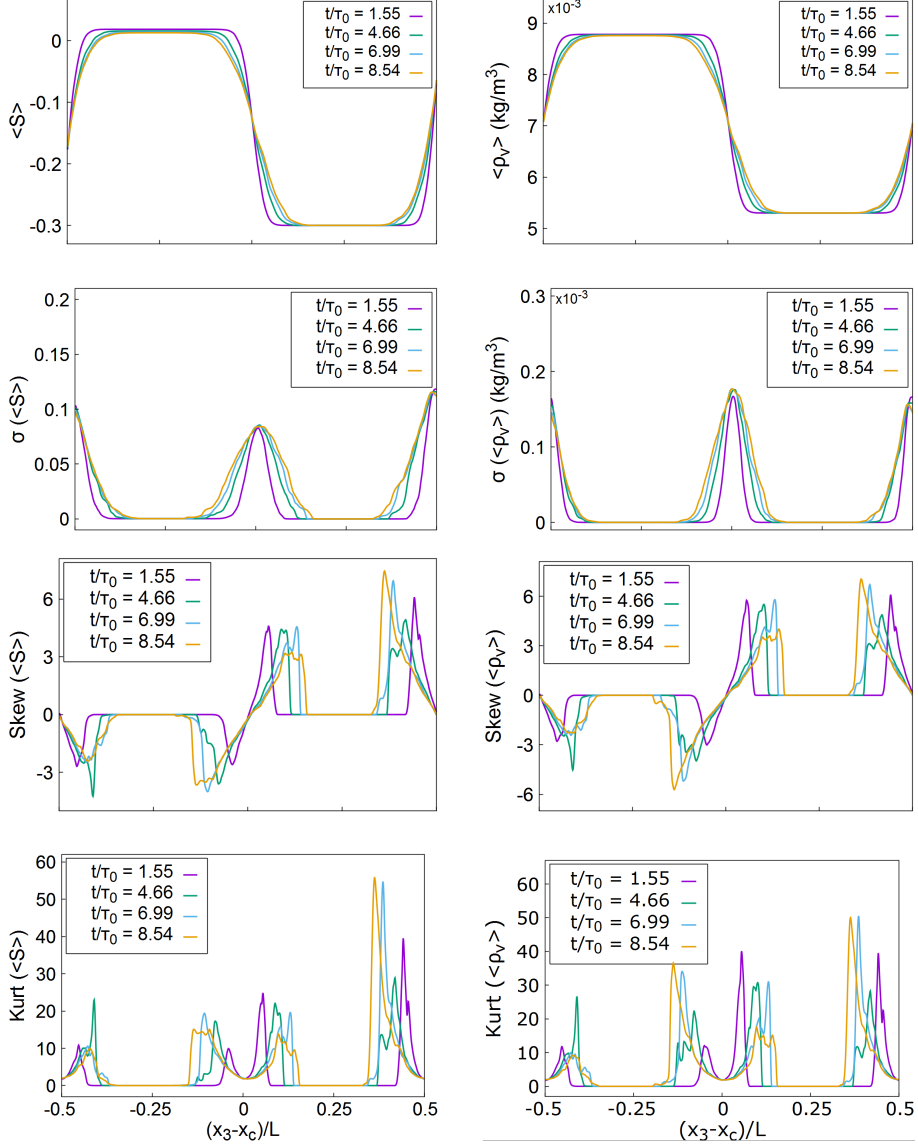


Figure 7: Statistical moments of the supersaturation and water vapor density fluctuations. Mono-disperse drop size distribution, unstable and time decaying cloud clear-air interaction. A practically identical situation holds for the poly-disperse distribution. When keeping constant the total liquid water content (LWC), this is due to the fact that the kind of distribution barely influence the background velocity and scalar fields.

ferent. Now, in the cloud region, all along the transient condensation is neatly prevailing on evaporation. Inside the interface layer, once again, evaporation

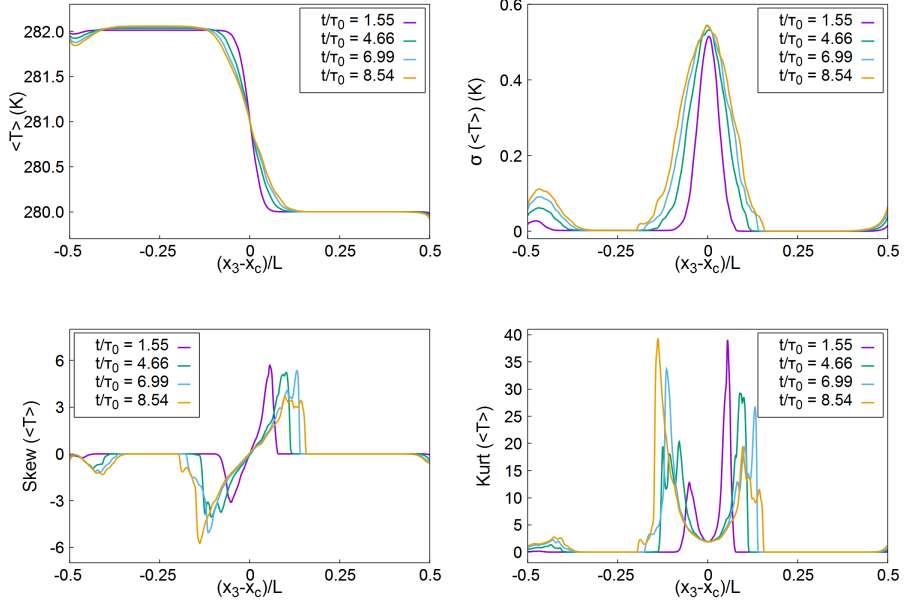


Figure 8: **Statistical moments of the temperature fluctuations.** Mono-disperse drop size distribution, unstable and time decaying cloud clear-air interaction. A practically identical situation holds for the poly-disperse distribution. When keeping constant the total liquid water content (*LWC*), this is due to the fact that the kind of distribution barely influence the background velocity and scalar fields.

prevail on condensation, but now in a weaker way. As usual, the more intense evaporation is present for the smaller drops where the curvature effect (the negative Kelvin term in the radius growth rate equation (14)) plays an important role. Here, we observe an evaporation rate about three times more intense than the condensation rate. One thing worth noticing is that in the interface both condensation and evaporation rates evolve non linearly in time, getting the maximum value around five eddy turn over times.

### 3.2. A comment on the droplet size distribution structure.

In the present situation of quick transient, where a rapid decay of the turbulent energy is taking place inside both the cloud region and the interface region characterized by an intense anisotropy, we should expect a system far from ergodicity. This is so for both drop populations.

It should be noted that the information conveyed by the drop size distributions are not sufficient to highlight the quantitative details of the condensation-evaporation processes that are instead visible from the analysis shown in previous figures 11, 12. However, size distribution structure variation are useful to get an overall view of the population evolution. In the following figures 13 and 14, we give quantitative data on the distribution shape, width, position and

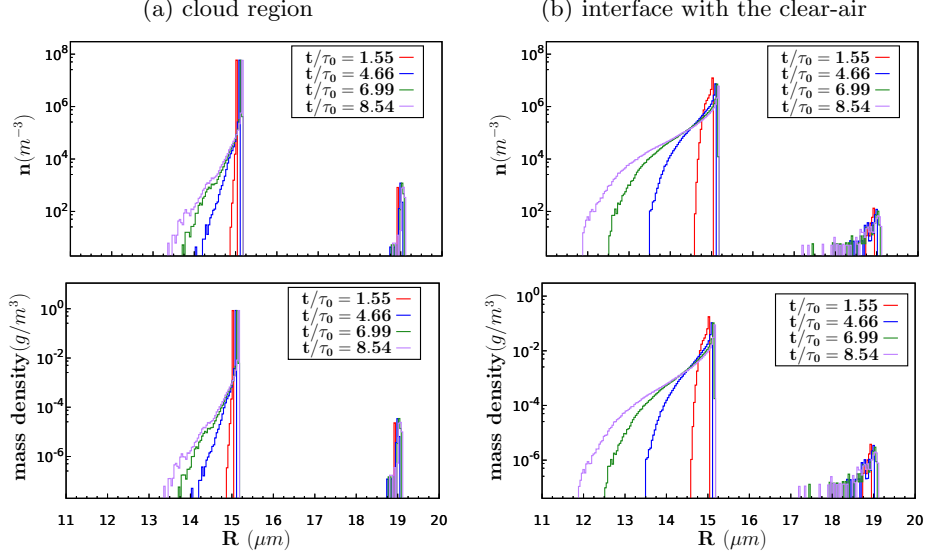


Figure 9: Water droplet size and mass distribution. Simulation of the monodisperse drop population centered around the initial value of  $15 \mu\text{m}$ ,  $8 \cdot 10^6$  droplets. Panel (a): droplet size distribution and mass distribution as a function of radius classes for the cloud region (HIT turbulence). Panel (b): droplet size distribution and mass distribution as a function of radius classes for the cloud and clear air/interface (shearless turbulent layer). See table 1 for physical and thermodynamical parameters, see table 2 for details on the numerical simulation parameters.

value of the maximum for the radii range where condensation and evaporation dominate. In practice, here, we neglect the coalescence between large particles that leads to radii larger than  $18 \mu\text{m}$  in the monodisperse case and larger than  $31 \mu\text{m}$  in the polydisperse case.

In the monodisperse case, figure 13, both inside the cloud region and interface layer, the distribution is highly skewed, see panels a) and b), where the distribution near the end of the transient is shown. The two distributions are different. In particular, their width is different. For the interface region the width is greater, nearly 5 time greater than inside the cloud region. We measured the time scale of the drop size standard deviation and, to enrich the information on the shape, we measured also the width of the distribution at a given percentage of the value of the distribution peak (0.03 %, where values are well readable), see panels c) and d). Both these quantities grow in time, but inside the interface the growth of the standard deviation is 13 times larger, while at the 0.03% of the peak value, the width is 6 times larger. The radius of the distribution peak slightly grows in time, more in the cloud region than in the interface; while the value of the concentration peak decreases, more rapidly in the interface, see panels e) and f).

For the polydisperse case, see figure 14. Here, trends are reversed. The

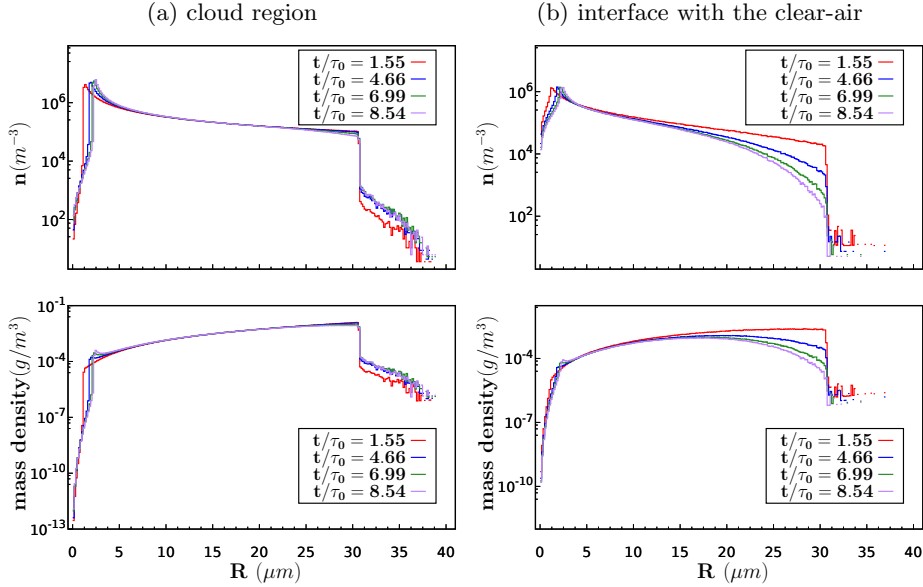


Figure 10: Water droplet size and mass distribution. Simulation of the polydisperse population with radii initially inside the range:  $0.6 - 30 \mu\text{m}$ ,  $10^7$  droplets. Panel (a) droplet size distribution and mass distribution as a function of radius classes for the cloud region (HIT turbulence). Panel (b) droplet size distribution and mass distribution as a function of radius classes for the cloud and clear air/interface (shearless turbulent layer). See table 1 for physical and thermodynamical parameters, see table 2 for details on the numerical simulation parameters.

concentration distributions are skewed in the opposite way, i.e. they enlarge with time towards the large radii side, see panels a) and b), where the distribution shape is shown near the end of the transient, again at about 7.8 eddy turn over times. The width of the distributions shrinks in time, more quickly (about 3 times) inside the interface region, see panels c) and d) where we include the information on the width of the distribution at a concentration equal to the 3% of the peak value. The radius of the peak of the distribution and its value grow in time both inside the cloud and inside the interface region, more or less in the same way.

#### 4. An approximated collision-coalescence kernel determination for the unsteady droplet aggregation inside an inhomogeneous turbulent layer

Collision kernels depend on the size of the colliding droplets, the kind of initial drop size distribution, and the process conditions and are used in the equations that govern the evolution of droplet size distribution which are referred to as population balance equations (PBE), see for instance [Kostoglou and Karabelas \(1994\)](#), [Vanni \(1999\)](#). Here, we would like to exploit our numer-

### Monodisperse droplets condensation and evaporation

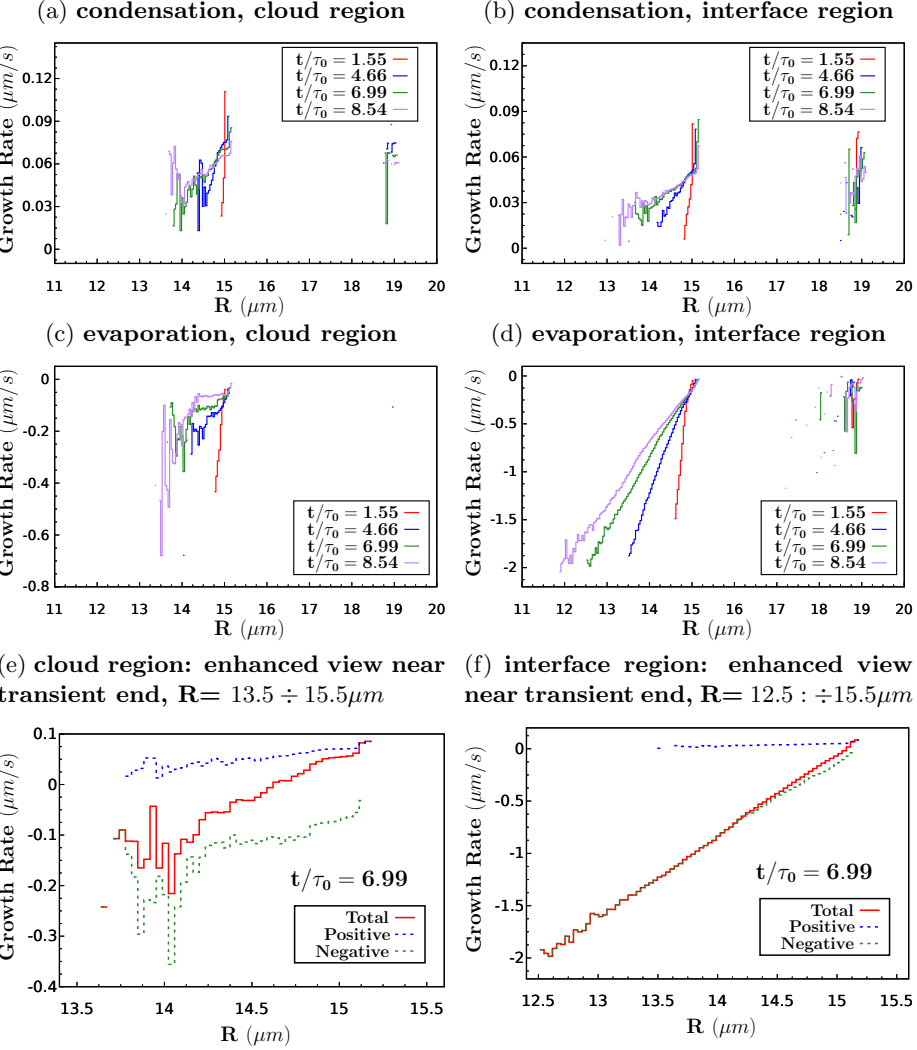


Figure 11: Monodisperse drop size distribution, unstable and time decaying cloud clear-air interaction. Mean droplet radius growth rate over different radius classes. Top panels: positive growth by condensation; central panels: negative growth by evaporation; bottom panels: resulting mean growth rate at selected time instant, computed on the entire population of droplets.

ical simulations to evaluate the possibility to compute a discrete approximate collision kernel for the droplet aggregation by the collisions-coalescence process which is taking place inside a turbulent airflow which is evolving in time and, simultaneously, is highly inhomogeneous. As seen above, this evaluation is carried

## Polydisperse droplets condensation and evaporation

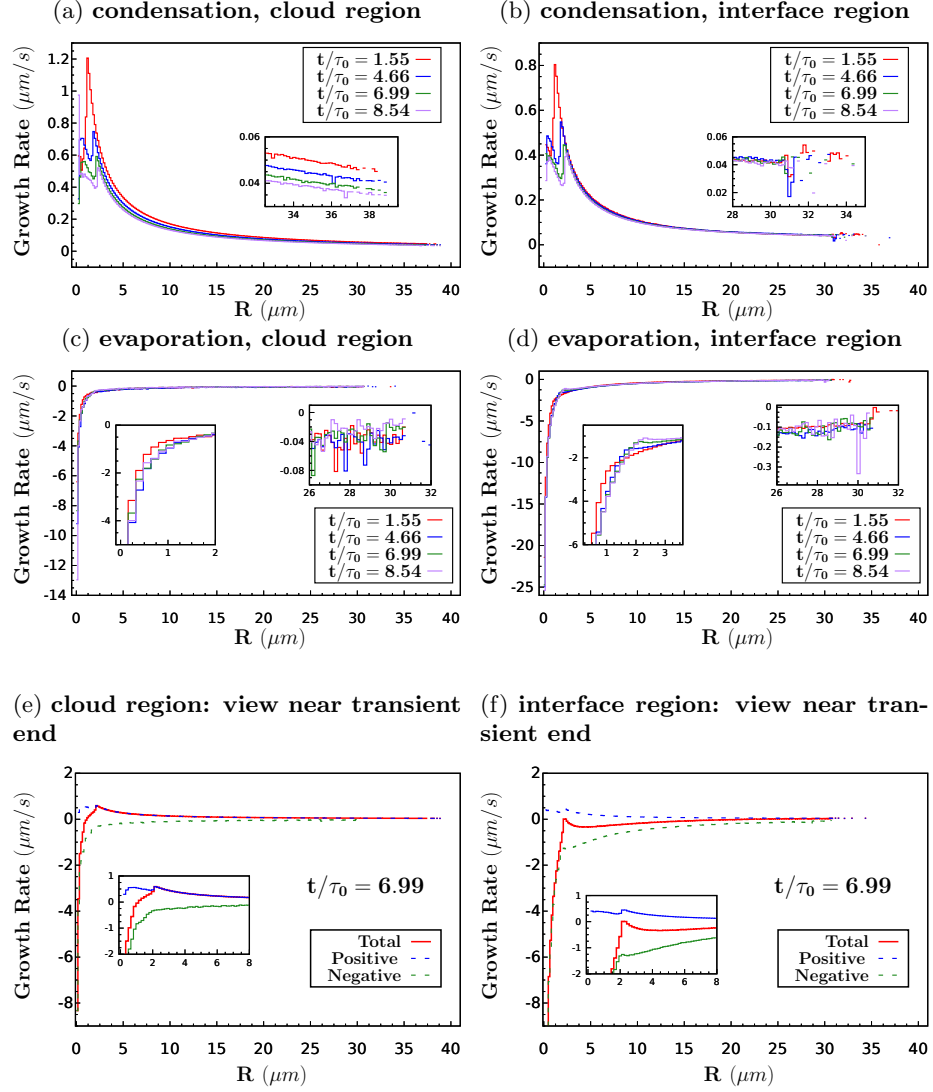


Figure 12: Polydisperse drop size distribution, unstable and time decaying cloud clear-air interaction. Mean growth rate over different radius classes. Top panels: positive growth by condensation; central panels: negative growth by evaporation; bottom panels: resulting mean growth rate at selected time instant, computed on the entire population of droplets.

out for two opposite initial size distributions (monodisperse and polydisperse with uniform mass). This comparison was made because, in the literature, the

### Monodisperse population size distribution

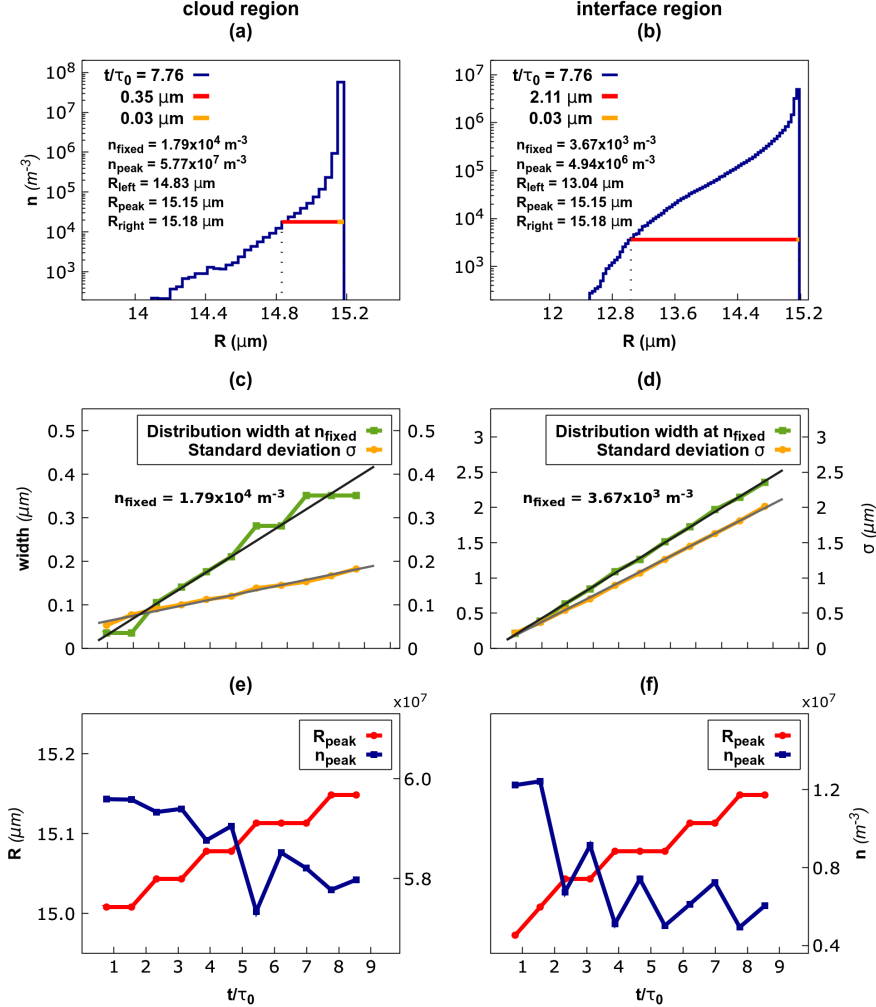


Figure 13: Mono-disperse drop size distribution, unstable and time decaying cloud clear-air interaction. Distribution characteristics. From top to bottom: left and right part of the distribution with respect to peak value for selected time instance (a,b); change of the distribution width over time (green) and its fit (black,  $0.047(t/\tau_0) - 0.006$  in cloud and  $0.28(t/\tau_0) - 0.02$  in mixing), standard deviation of the distribution over time (orange) and its fit (gray,  $0.015(t/\tau_0) + 0.05$  in cloud and  $0.23(t/\tau_0) + 0.003$  in mixing) (c,d); change of peak distribution value (blue) and corresponding radius class (red) over time (e,f).

typical form of the size distribution in warm natural clouds to refer with is not yet available and perhaps will not be available in the near future.

### Polydisperse population size distribution

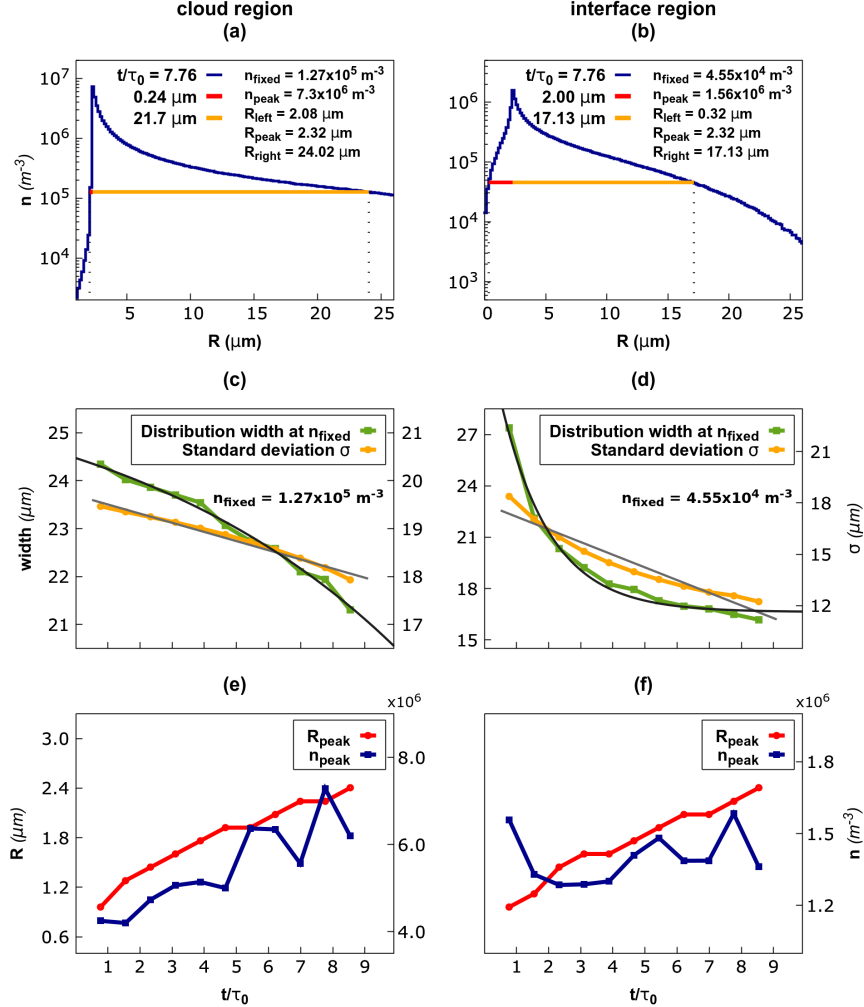


Figure 14: Poly-disperse drop size distribution, unstable and time decaying cloud clear-air interaction. Distribution characteristics. From top to bottom: left and right part of the distribution with respect to peak value for selected time instance(a,b); change of the distribution width over time (green) and its fit(black,  $26.47 - 2 \exp(0.11(t/\tau_0))$  in cloud and  $16.62 - 17.23 \exp(-0.67(t/\tau_0))$  in mixing), standard deviation of the distribution over time (orange) and its fit (gray,  $-0.19(t/\tau_0) + 19.69$  in cloud and  $-0.74(t/\tau_0) + 17.94$  in mixing) (c,d); change of peak distribution value (blue) and corresponding radius class (red) over time (e,f).

In such a fully non-ergodic condition, we aim at giving a first preliminary data set on the statistical convergence reachable by using the popular approach

where the drop size spectrum is approximated by a set of size classes.

In literature, the common scenario for studies of turbulent flows laden with solid particles or liquid droplets is the steady-state homogeneous isotropic turbulence. Related contributions, including the context of atmospheric cloud physics, are numerous and by now a few of them became historically important. Let us summarize shortly the situation. One of the pioneering theory has been proposed by [East and Marshall \(1954\)](#). These authors discussed the turbulence as equivalent, in its effects, to a random motion in time of the whole air parcel containing all drops, neglecting any spatial variations. A remarkable result they found is that equal drops rarely collide. A few years later, [Saffman and Turner \(1955\)](#) considered collision between small drops of similar size in a homogeneous, isotropic, statistically stationary turbulent flow. They considered both drops moving with the air (zero inertia particles) and relative to the air, in the presence of gravity. The distribution of drops was random and uniform. Since homogeneous and isotropic turbulence was considered, the resulting collision rate could be presented in terms of the dissipation rate of turbulent kinetic energy and of the viscosity (as well as the radius of each drop). More recent research has shown that the drop concentration in turbulent flows may be highly non-uniform with local regions of anomalously high or low concentration. In fact, the coherent vortical structures in real turbulent flow are the mechanisms that brings about preferential concentration by producing directed (non-random) motions of particles. This kind of dynamics is frequently observed in gas flows laden with solid particles or liquid drops and is related to the great difference in density between the carrier flow and the filling particles. The variations in particle concentration are far greater than would be expected from statistical considerations. This raises serious concerns about the utility of statistical models to represent particle-laden turbulent flows, [Eaton and Fessler \(1994\)](#)).

Preferential concentration means that liquid drops cannot generally follow whirling curved streamlines and thus spirals away from the center of the vortex. It is then expected that vortex cores would be regions of low droplet concentration; a fact confirmed by numerous experiments and simulations. On the contrary, it is seen that a typical droplet entering a region characterized by high strain rate and low vorticity crosses curved streamlines. In this case, a high concentration of particles is observed in these low vorticity regions, which is again confirmed by experiment and simulation ([Maxey \(1987\)](#), [Ruetsch and Maxey \(1993\)](#), [Reade and Collins \(2000\)](#), [Vaillancourt et al. \(2001\)](#), [Vaillancourt et al. \(2002\)](#), [Petersen et al. \(2019\)](#)). Another effect is related to droplet-droplet aerodynamic interactions, which affect the collision efficiency [Lanotte et al. \(2009\)](#). Because of the complexity of the problem [Ayala et al. \(2013\)](#), there are only a few Direct Numerical Simulation (DNS) studies concerning this last effect ([Wang et al. \(205\)](#), [Ayala et al. \(2007\)](#), [Ayala et al. \(2014\)](#)). Most of these treatments are still under development. In the Lagrangian model of droplet transport and collision used here this effect is not considered.

Let us now come back to the collision kernel exploration done on our direct numerical simulations. The analysis is actually performed on a perturbed

shearless turbulent layer where a mild unstable stratification is active on either the monodisperse or the polydisperse population of droplets. In this second case, given the concomitant presence of very different droplets, the volume ratio between the largest to the smallest is of the order of  $1.25 \cdot 10^5$ , the number of collision will be large. Out of  $10^7$  total droplets, we in fact observe about  $5 \cdot 10^4$  collisions over about 10 physical time scales.

The turbulent process for which we measure the collision kernel tries to mimic a real small initial perturbation of the interface cloud clear-air. The process includes the effects of the non-stationariness, anisotropy and inhomogeneity of the fluctuations, which of course includes inertial effects, the condensation-evaporation growth-decay of the drops and the gravitational stratification and settling. We remind that the collisions must be viewed as geometric since the Stokes' drag was included in the momentum equation of the particle, however, droplet - droplet local aerodynamic interactions are not included. Thus we assume a collision efficiency equal to unity. Another minor simplification is that the coalescence efficiency, which is defined as the ratio of the number of actual merged drops and the total number of collisions, is taken equal to unity. However, laboratory studies of colliding cloud droplets have shown that coalescence efficiency is near unity ([Woods and J. \(1965\)](#) and [Beard et al. \(2002\)](#)). In our investigation, the initial liquid water content (*LWC*) is  $0.8 \text{ g m}^{-3}$ , a close value to the typical adiabatic value found in cumulus clouds. We computed the collision kernel from our simulation as:

$$\Gamma(R_1, R_2; t, \mathcal{V}) = \frac{N_{\text{coll}}}{n_1 n_2} \frac{\mathcal{V}}{(t_2 - t_1)}, \quad (17)$$

where  $N_{\text{coll}}(R_1, R_2, t \in [t_1, t_2])$  is the counter of collisions between droplets of radius  $r_1$  and  $r_2$ , occurred during a selected time window  $[t_1, t_2]$  and within a selected spatial region of volume  $\mathcal{V} = L_1 \times L_2 \times \Delta x_3$ . In the denominator,  $n_1$  and  $n_2$  are the counters of **all droplets** within the class size where  $R_1$  and  $R_2$  are met, for the same temporal range and spatial volume. See, for example, equation (3) in [Vanni \(1999\)](#). All counters are obtained from a uniform radii discretization. This computation is approximated because  $n_1$  and  $n_2$  approximate the counters of particles of radius  $R_1$  and  $R_2$  in the limit for  $\delta R \rightarrow 0$ . We performed a set of computations by subdividing the radius range, the range  $[0.6 - 30] \mu\text{m}$  in the case of the polydisperse population, into 16 classes and up to 512 classes, which means from a  $\delta R = 2.5 \mu\text{m}$  to a  $\delta R = 0.078 \mu\text{m}$ . Consequently, by means of an ensemble averaging over three realizations of simulation data, a convergence analysis was performed, see figures 15, 16, and the synthesis shown in figure 17.

By working within the numerical double precision, when using a subdivision in 512 classes, we obtained a good convergence on the number of droplet collisions, but there we started having problems of rounding errors on the value of the kernel, see figure 16. Values less than  $10^{-13}$  cannot be computed. By extrapolation, we see that convergence can be reached by subdividing our radii range in  $10^6$  classes. That is by passing from about  $2^{10}$  classes to  $\sim 2^{20}$  classes, a performance that even within the quad-accuracy could be difficult to achieve.

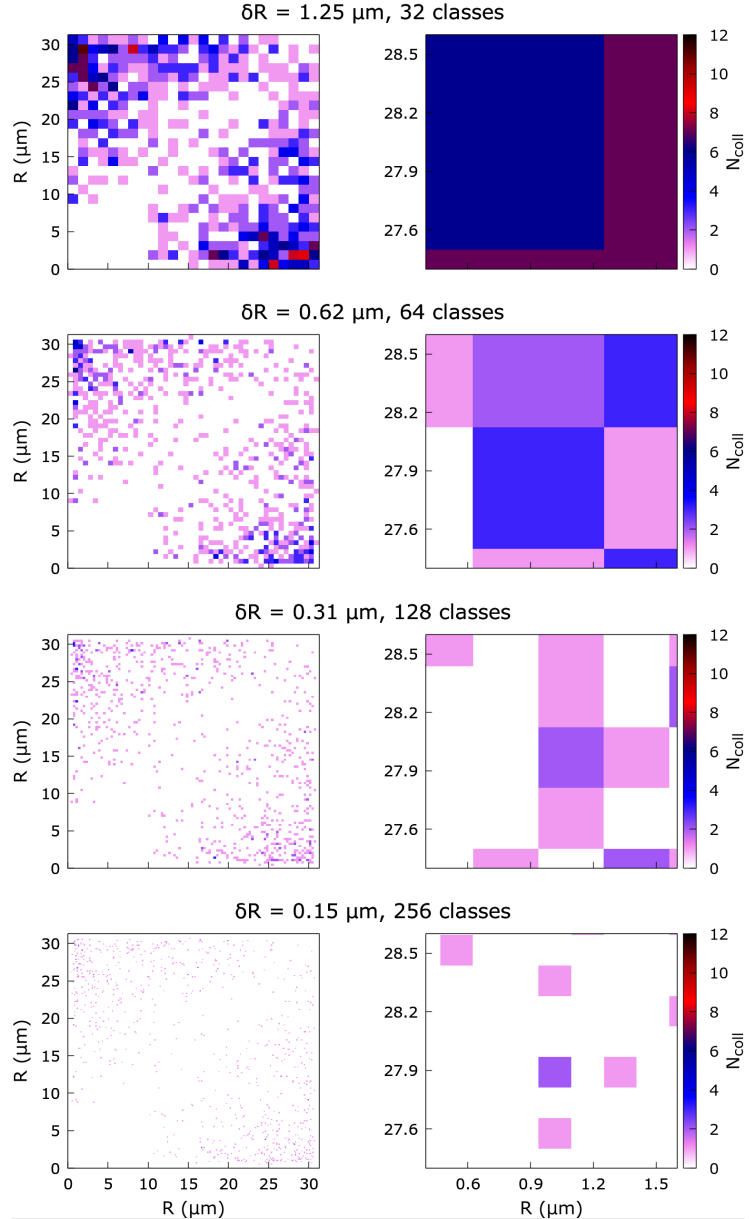


Figure 15: Convergence on the number of collisions inside the cloud/clear-air interface region within the time interval  $t/\tau_0 = [0 - 0.8]$ . The analysis is shown for different dimensions of the radius classes, starting from 32 up to 256 classes. The four right panels ( $R_1 \in [0.4, 1.6] \mu\text{m}$ ,  $R_2 \in [27.4, 28.6] \mu\text{m}$ ) represent a zoom of the left four panels where  $R_1, R_2 \in [0, 31.5] \mu\text{m}$ .

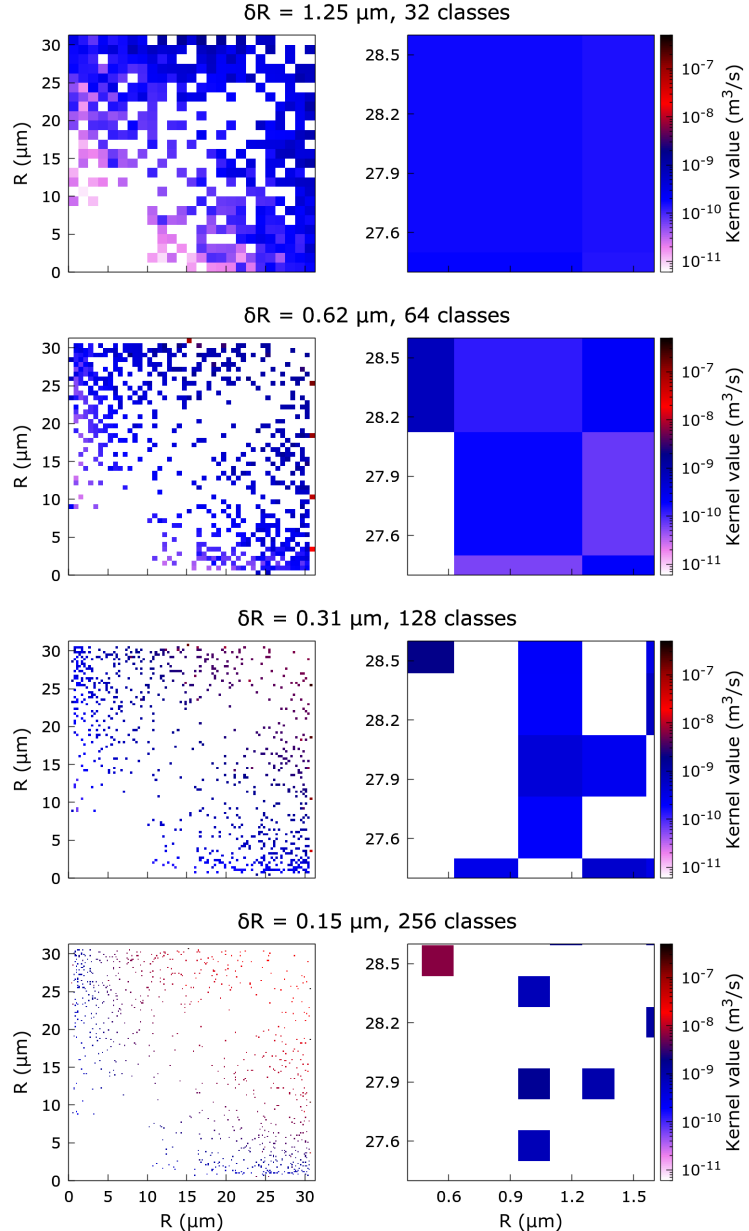


Figure 16: Polydisperse drop initial distribution. Convergence on kernel values inside cloud/clear-air interface region within the time interval  $t/\tau_0 = [0 - 0.8]$ . The analysis is shown for different dimensions of the radius classes, starting from 32 up to 256 classes. The four right panels ( $R_1 \in [0.4, 1.6] \mu\text{m}$ ,  $R_2 \in [27.4, 28.6] \mu\text{m}$ ) represent a zoom of the left four panels  $R_1, R_2 \in [0, 31.5] \mu\text{m}$ .

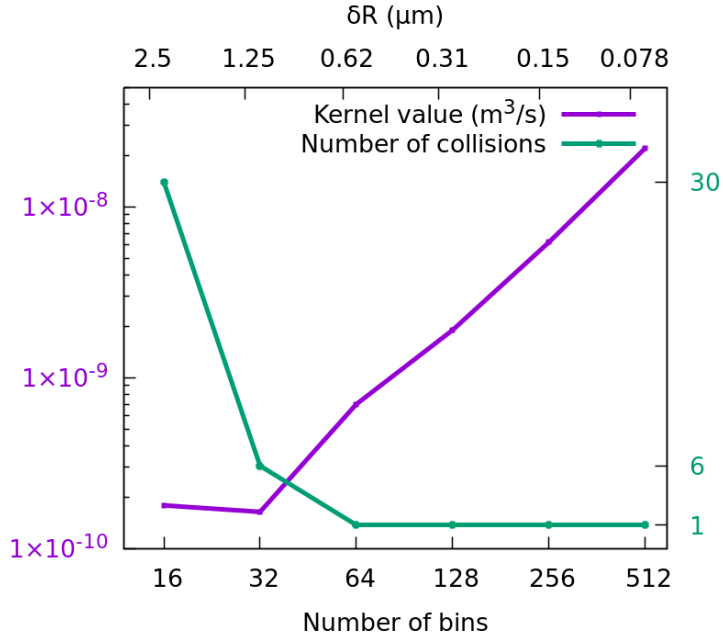


Figure 17: Convergence of number of collisions and kernel values inside mixing region. Data refer to  $t/\tau_0 = [0.0 - 0.8]$   $R_1 = 28.59 \pm \delta R/2$  and  $R_2 = 0.47 \pm \delta R/2$  and can be considered significant for the entire system, though convergence is not uniform in the field.

As a future investigation, we consider worthwhile a comparative analysis of the performance attainable by the present methods and methods like the one used in the context of molecular gas dynamics applied to the Direct Simulation of Gas Flows. For instance, by applying the direct simulation Monte Carlo (or DSMC) method that has, in recent years, become no longer expensive and consequently is widely used in engineering and scientific studies of gas flows that involve low densities or very small physical dimensions.

We analyzed the kernel time evolution over intervals of width comparable with the turbulence eddy turn over time computed at the beginning of the simulation,  $\tau_0$ . The observation starts from the initial instant until about  $10\tau_0$ . For the polydisperse drop size initial distribution, since over the entire time evolution we get 50000 collisions, this implies about 5000 collisions per interval. Over the evolution, we analyze the variation of the number of collision inside the cloud portion and inside the interface. In the light of a future simulation campaign, this allow to estimate the number of realizations needed to get an effective estimator of the ensemble average of the kernel value.

Let us start the results description by considering in figure 18 the collision kernel values for the polydisperse population computed inside time intervals as wide as one third of the transient decay. In the left column we have the interface values, in the right column the cloud values, drop radii are classified

in 256 ranges. The top panels, the first third of the transient, own about 10400 collisions on 10 million of drops. About one fourth of collisions take place inside the interface. One can appreciate that practically anywhere inside the pixelated matrix the values of the kernel values inside the interface are higher than in the cloud portion. Kernel value levels are not sharply contoured. In fact, we can see wide portions of the matrix where an intense and discrete (pixelated) merging of values that differ by one or more orders of magnitude is observed. This remain true for the other two thirds of the transient where the main difference is the increase of the number of collisions inside the interface at the expenses of the number of collisions inside the cloud. At the end of the transient, bottom panels, the collisions inside the interface are more numerous than inside the cloud (4179 versus 3824). In figure 18, outside the initial drop radii area  $[0-30]\mu\text{m} \times [0-30]\mu\text{m}$ , we can see points (pixels) that represent drops resulting from a possible double or triple sequence of collisions, see also figures 10 and 12. Values here are maximal ( $1 \cdot 10^6$ ) and are accurately determined because the concentration of the drops with radii equal to that of collided drops are automatically accurately computed. This because drops with other radius but in the same class are here scarcely present. It should be noted that the number density of collisions (number of collisions divided by the volume) inside the cloud region nearly remain constant in time concurrently with the decay of turbulent kinetic energy. More interesting, however, is the situation inside the interface region which is expanding both in the simulation and in the real system. Here, notwithstanding the intense energy decay, see figure 2, the absolute number of collisions inside the interface layer grows, while the volume density of collision slightly decay of nearly a 30%. We will come back later on this aspect by commenting on the collision correlation with the velocity and passive scalar fluctuation intermittency.

Considering now the situation for the initially monodisperse drop population, we observe a dramatically lower number of collisions - a thing attended given that initially drops are identical. See figure 19, where the total number of collision along the entire transient is about 400 out of the 7 million of drops introduced in the system to reach the total liquid water content for warm cloud ( $LWC = 0.8 \text{ g/m}^3$ ). Inside the cloud region, the number density of collisions decays of the 76% along the transient. This happens concurrently with the decay of the kinetic energy of 92%. The absolute number remains instead constant inside the expanding interface region where drops undergo a rapid evaporation. This corresponds to a decay of the 50% in term of the number density concurrently with a 86% decay of kinetic energy. It is evident, that within the initially monodisperse population dynamics, the collision activity is very minor with respect to the condensation-evaporation dynamics. Actually, the information that can be derived from this analysis is the diagonal and lateral spreading on the radii range where information is available. From this set of simulations and the actual ensemble averaging, as preliminary information, we can deduce a diagonal spreading of about 18% per eddy turn over time, and a lateral spreading of 25%. To put forward a simulation campaign leading to an ensemble averaging based on a number of collision events of the order of a few thousands, a number

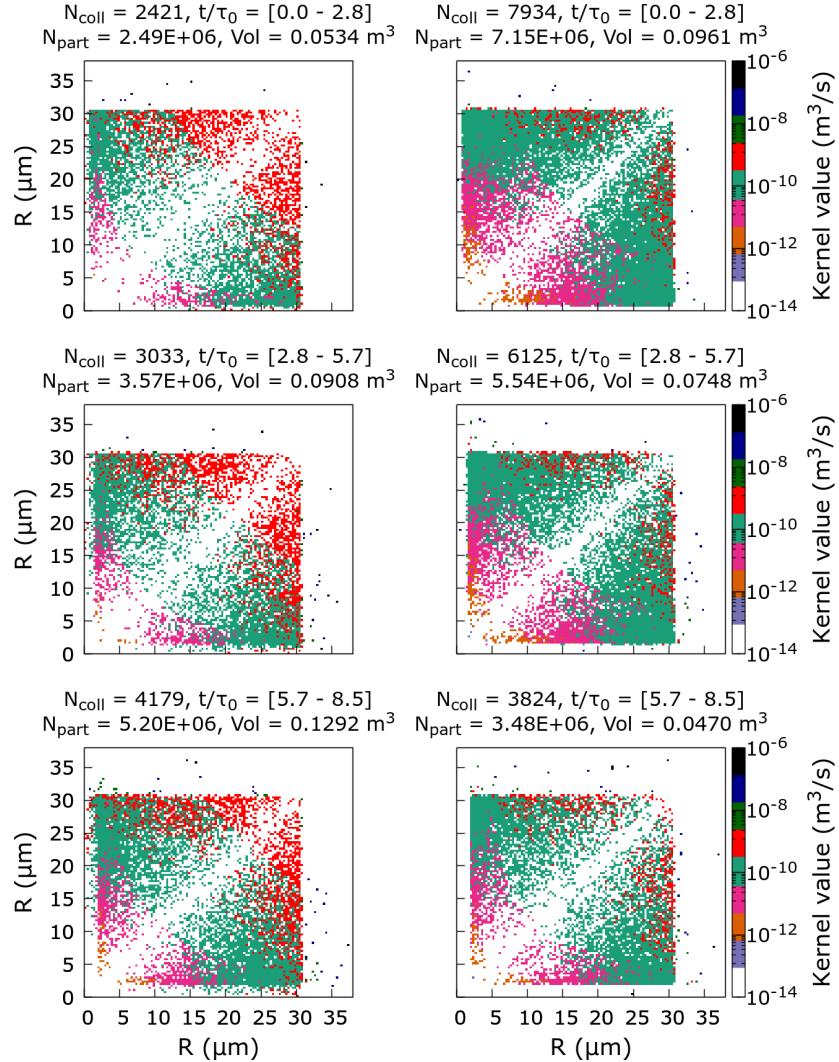


Figure 18: Polydisperse drop size distribution, unstable and time decaying cloud clear-air interaction. Comparison of kernel value evolution inside the cloud-clear air interface (left) and the homogeneous cloud region (right). Ensemble average obtained over three realizations of simulation data, mean evolution over time intervals as long as one third of the entire observed decay. Collision radii subdivided into 256 classes.

of realizations of the order of 100-200 is needed.

By observing the temporal evolution of the polydisperse population within shorter intervals, the kernel morphology disclosed by the 256 radii classes computation appear to be layered, see figures 20 and 21. The peak values are concentrated in the lateral corners where the collisions take place between the smallest

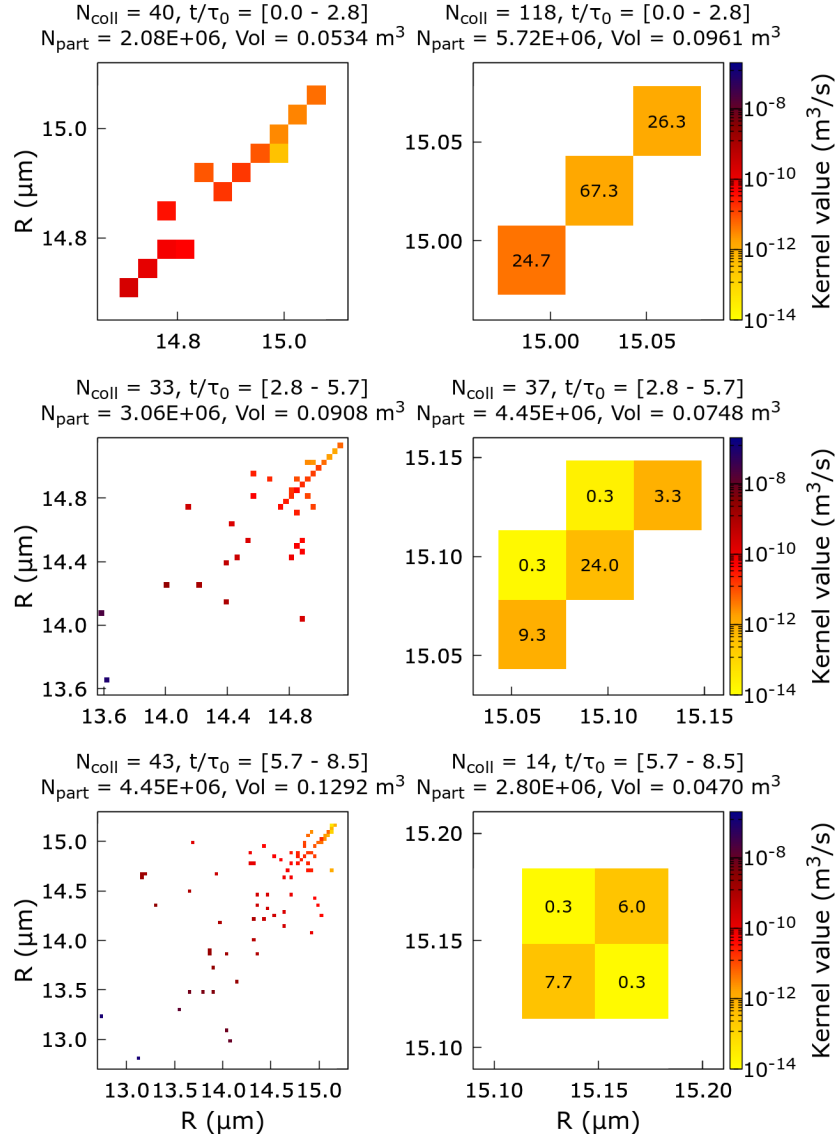


Figure 19: Mono-disperse drop size distribution, unstable and time decaying cloud clear-air interaction. Comparison of kernel value evolution inside the interface region (left) and the cloud region (right). Ensemble average obtained over three realizations from simulation data.

and the largest droplets. Intermediate values pertain to collision between large drops. Minimal values to collisions between small drops. Zero probability for collisions among same radius drops, for any radius value. This trend apply both to the interface and the cloud regions. But in proportion values inside the cloud

homogeneous region are lower, in general, by less than one order of magnitude. A reasonably sufficient number of realizations to get a statistical base of a few  $10^4$  events would be 10-20.

A comment is here opportune. The polydisperse population here considered was build according to a criterium based on the uniform mass distribution. This choice was induced by the wish to observe a population where the collision rate could be expected large because a high density of small droplets was co-present with droplets about 30000 times larger. However, this distribution is physically not a probable distribution, which means that when using more physical conditions - not yet fully known as far the in-field droplet size distributions are concerned - the collision rate should be expected lower. This arises the number of realizations needed to produce sufficiently good kernel statistics. In this regards, the reader can be interested in the reading of the very recent paper by [Chandrakar et al. \(2020\)](#), where an accurate laboratory experimental evaluation of various theoretical distributions is made.

Eventually, we would like to briefly discuss the previous results compared to the very popular theory of Saffman and Turner (1965), hereinafter referred to as the ST model. This model is still a reference of general interest in the field of the engineering of multi-phase turbulent flow systems. The Saffman and Turner model holds for a background turbulence which is steady state, homogeneous and isotropic. A situation thus far from the system conditions we are studying here. That is a situation characterized by an unstable density stratification and transient decay of an inhomogeneous and anisotropic shearless turbulence which is mimicking the interaction between a warm cloud portion and the clear air bounding it. Anyway, at present, the literature does not present kernel statistics for collisions hosted by an anisotropic turbulence in temporal decay and thus this kind of comparison can be useful to highlight differences between a near ergodic and a fully non ergodic system.

The comparison is presented in figure [22](#), where the three contributions inside the ST model are contrasted, namely, i) collision rate due to different particle inertia because of the action of the turbulent acceleration, term A, ii) action of gravity, term B, and iii) collision rate due to the spatial variation of turbulence air velocity, term C. It should be recalled that ST model is not parameterized with the Reynolds number, which is anyway hypothesized very large. It can be noticed that in this model, for  $\epsilon = 10 \text{ cm}^2/\text{m}^3$  and an air temperature of 280 K, the collision between drops moving with the air, term C, is playing a minor role with respect to terms A and B. The two bottom panels of figure [22](#) show the comparison of the ST model with the kernel computed for the polydisperse droplet population case studied in our non ergodic simulation. The comparison is done inside a portion of the transient where the dissipation value is not far from the value inserted in the ST model. One can appreciate the large difference in the kernel values, which reaches many orders of magnitude. The values seen in the simulation are close to the lowest values shown by the ST contribution C, i.e. the contribution due to the collision between droplets moving with the air. The shape of the kernel is also different. However, to deduce a quite accurate kernel morphology in non ergodic non homogeneous conditions it is

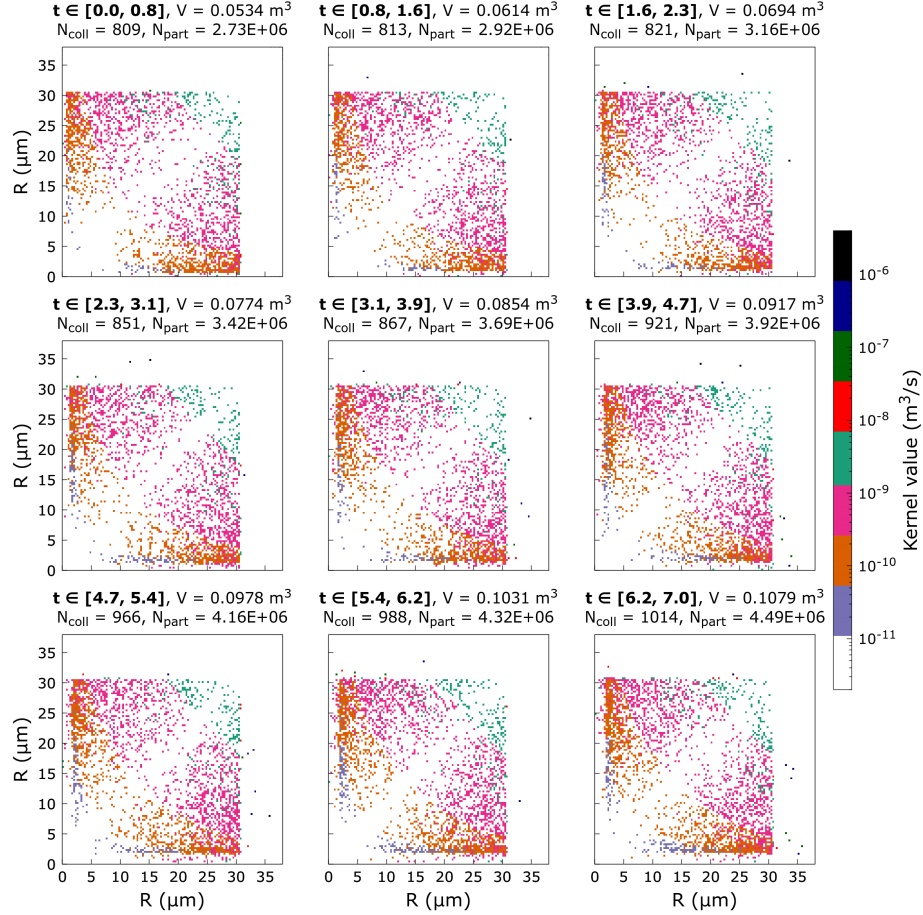


Figure 20: Poly-disperse drop size distribution, unstable and time decaying cloud clear-air interaction. Kernel value evolution over time inside the interface region. 128 radii classes. Ensemble average over three realization simulation data.

necessary to carry out a sufficient number of ensemble averages. In the case of the widely dispersed population in which the probability of droplet collision was conditioned to be high, we estimate a sufficient number of ensemble averages such as 10-20. Which is a number that should produce statistics greater than  $10^4$  collision events. In the opposite case of the monodisperse population, the number of ensemble averages to obtain statistics on at least  $10^3$  collision events should be around 100-200.

#### 4.1. Small scale turbulent velocity fluctuation and collision count correlation.

We end the results description by a short comment on the correlation between the fine scale of the turbulence and the collision count observed inside the

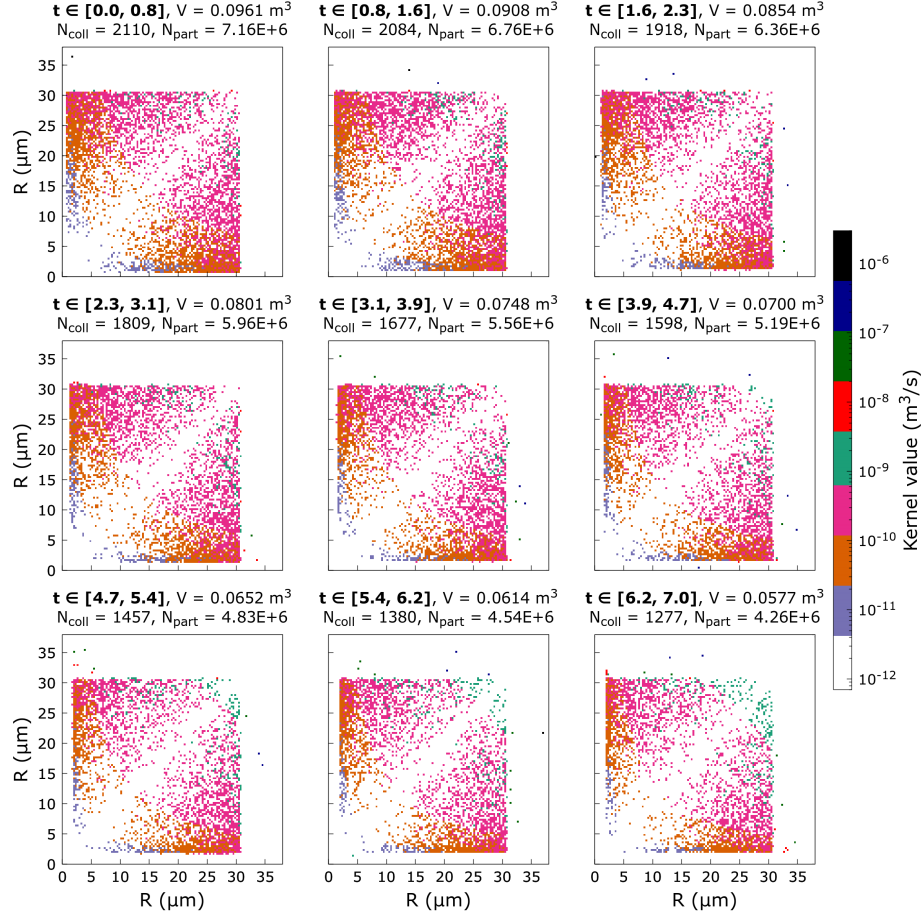


Figure 21: Poly-disperse drop size distribution, unstable and time decaying cloud clear-air interaction. Kernel value evolution over time inside the homogeneous cloud region. 128 radii classes. Ensemble average obtained over three realizations of simulation data.

simulation of the polydisperse droplet population evolving inside the interface between the cloud and the clear air environment. As part of the microphysics dynamics, droplet collisions is naturally correlated with the small inertial and the viscous microscale of the turbulence. In fact, one can see from the statistical moments and collision count in figure 23, and from the correlation index (Pearson correlation index, Teukolsky et al. (1992)) shown in figure 24 that, inside the cloud region, the correlation index reaches the extremely high value of 0.9 - 0.94. Less obvious is the fact that the correlation index is still very high, not far from the value of 0.5, inside the interface. And throughout the simulated temporal decay. In fact, in the interface the small scales of the velocity field are very anisotropic, despite the lack of a mean shear velocity flow. Furthermore,

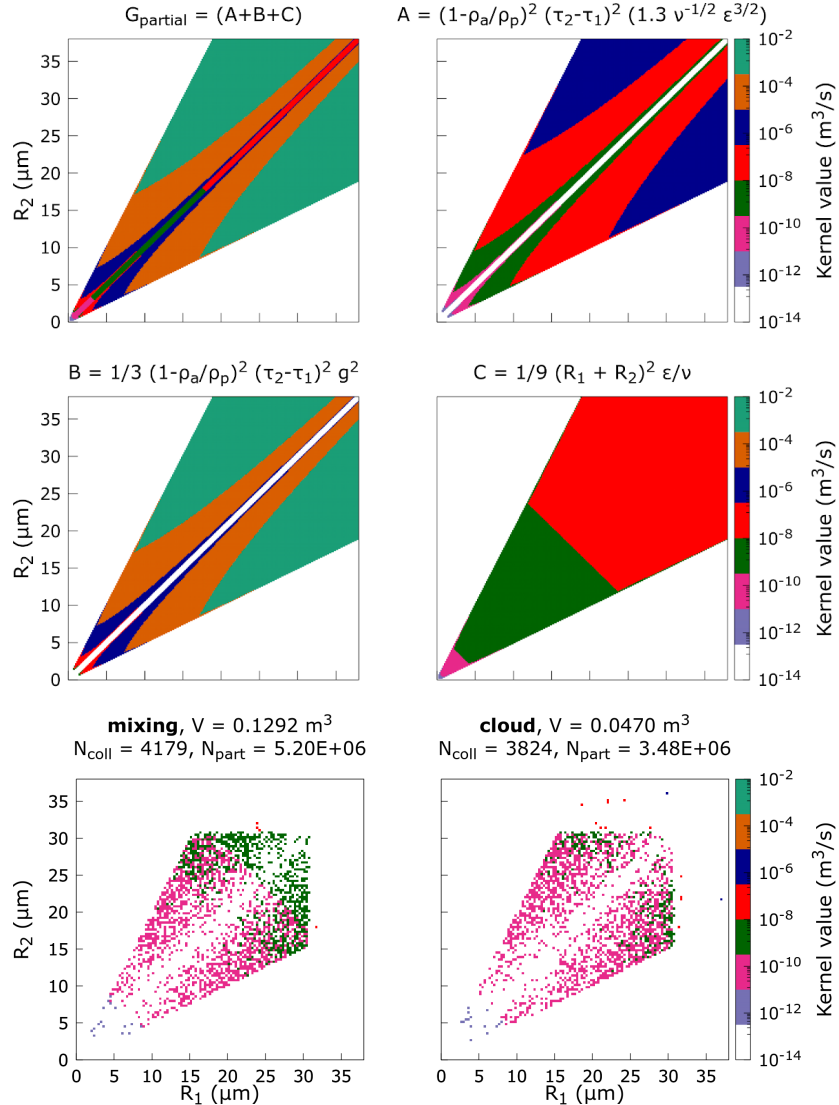


Figure 22: Comparison between the analytical Saffman and Turner model (valid for steady state homogeneous isotropic turbulence, constant dissipation:  $\epsilon = 10 \text{ cm}^2/\text{s}^3$ ,  $R_1, R_2 \in [0, 38] \mu\text{m}$ ,  $R_1/R_2 \leq 2$  and  $R_2/R_1 \leq 2$ ) and our simulation (unsteady, inhomogeneous anisotropic) on kernel statistics in a transient lapse where the dissipation has a comparable value, that is  $t/\tau_0 \in [5.7, 8.5]$ . In the upper 4 panels one can see the different terms of Saffman and Turner model for the given dissipation. The portion of the  $R_1, R_2$  graph where the model is valid is only considered. The two bottom panels show kernel statistics for the polydisperse simulation. Left, mixing interface, right, cloud region. These data are the same of the bottom two panels of Fig. 18, shown inside the validity region of the ST model.

they are in any case rapidly decaying due to viscous dissipation. This show how water droplet growth by coalescence due to collision can still take place at the cloud border.

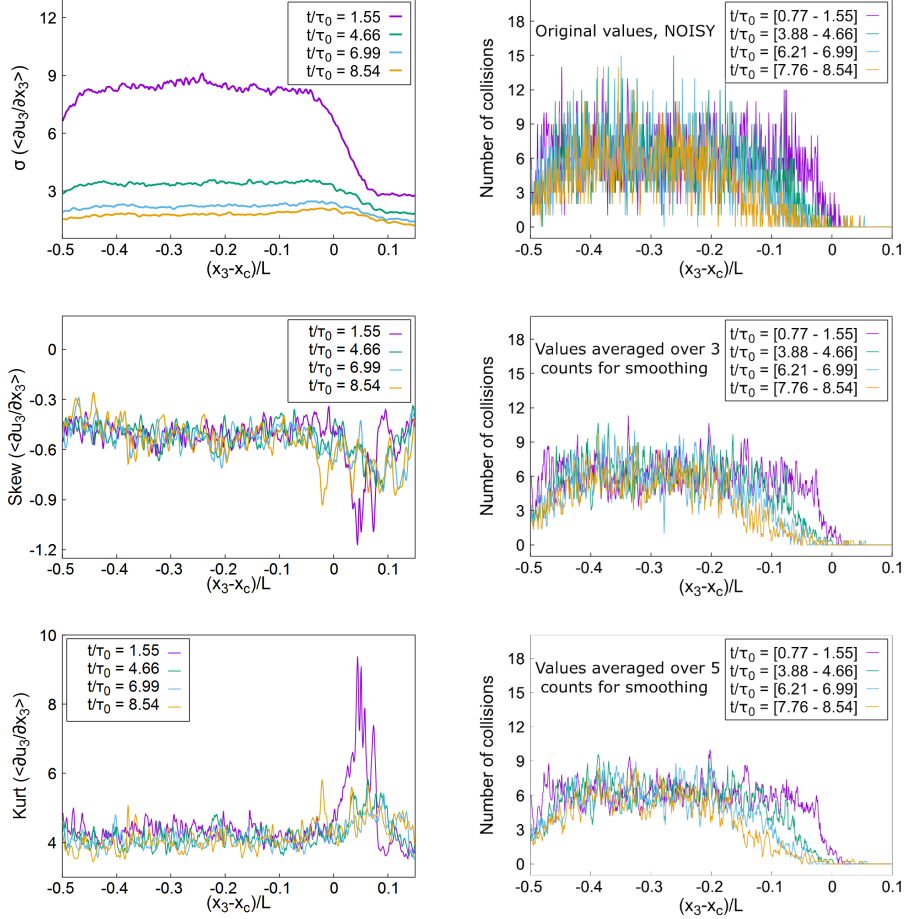


Figure 23: Poly-disperse drop population, unstable and time decaying cloud clear-air interaction. Second, third and fourth statistical moments of the fluctuation of longitudinal velocity derivatives of the background velocity field (left) and number of collisions along the vertical direction (right). In the left panels, the homogeneous portion of the domain (cloud region) and the interface region are showed. Ensemble average obtained over three realizations. For the collision number, we show the averages over each computed section (noisy data, top right panel), and over three (middle right panel) and five adjacent sections (bottom right panel).

## 5. *Conclusions and outlook*

In this paper, we present the results of a set of numerical simulations focusing on the interaction of the turbulent cloud environment with the surrounding clear air ambient. It has not been intended that the results should reproduce the events which may occur in a particular cloud but rather to loosely reproduce a simplified portion of a warm cumulus cloud. Rather, the results should highlight both the positive aspects and the problems met while working with models where the dynamical and microphysical properties of cloud boundaries are joined.

We have carried out calculations based on the Navier-Stokes air flow turbulence which is hypothesized to be present both inside the clouds and the interfacial turbulent layers separating them from the surrounding clear air. These layers are modelled as unstably stratified shearless mixings.

This background air motion is hosting both water vapor and water droplets. The system is basically an incompressible fluid system governed by Eulerian equations describing the velocity, temperature, and water vapor fields under the Boussinesq approximation. This set of equations is coupled to the Lagrangian equations describing the motion of the inertial droplets which are subject both to the Stokes drag and the gravitational settling. This is a one-way coupling approach and does not include the feedback from the droplet motion to the air-flow field. The originality of this study consists in having considered a physically common in nature, however non ergodic, condition of interaction between cloud and clear air. This condition has been applied to two different types of water drop population. The case of a population containing drops initially having the same diameter, a situation in which collisions are in fact unlikely, and the case of a population of drops with very different radii, which, on the contrary, is biased to host collision events. In both cases we have included in the computational domain a number of drops in the order of 10 million, a sufficient number to reproduce the real values of the liquid water content of the warm clouds.

In the monodisperse case, we observed a powerful evaporation of the drops accompanied by a low level of growth by condensation. This induces a rapid droplet spectral broadening that in turn produces collision events. The position of the peak of the distribution of the number of drops smoothly shifts towards diameters greater than the initial one, a fact which is not intuitive. Instead, as expected, the peak value decreases. We provide quantitative data on these trends. The collisional activity of the drops becomes more intense within the air-cloud interface. Here, the evaporation is immediately active on collided particle, a thing which does not happen inside the cloud region. Overall, inside the interface region evaporation and collision prevail over condensation.

In the polydisperse case, the droplet size distribution is wide from the very beginning of the simulation. The distribution broadening is thus due to the collision events only. The evolution tendency is clearly that to become a peaked kind of distribution, where the position and value of the peak depends on the structure of the turbulence hosting the droplet population. The width of the distribution decreases while both the radial position and the numerical concentration of the peak grow in time. We give quantitative figures for these trends.

An interesting thing is that much of the evaporation and condensation dynamics for this kind of population is taking place at the lowest boundary of the droplet spectral range. Inside the cloud region, all along the transient condensation is neatly prevailing on evaporation. Inside the interface layer, once again, evaporation prevail on condensation, but now in a weaker way.

The collision kernel analysis has shown a clear dependence on the evolution time and on the spatial region, and related turbulence structure where collisions take place. The statistics obtained by means of ensemble averaging over three simulation repetitions highlight the necessity to foresee another campaign of simulations that can lead to an effective interpolation of the kernel values for the considered population drop radii range. This in order to provide an analytical model of the collision dynamics in conditions far from ergodicity. Our evaluation provides a number of 20 simulation repetitions for the case of the multidisperse population and of 100-200 repetitions for the monodisperse population. The comparison with the Saffman-Turner model, valid for an almost monodisperse population in conditions of stationary and isotropic turbulence, as could be expected, is not positive. By placing ourselves in conditions of equivalence on the only dynamic parameter present in the Saffman-Turner model, the dissipation of turbulent energy, we observe in our simulation kernel values of many orders of magnitude lower with respect to ST. The morphology is also different. In our preliminary observations we see a band structure and not a butterfly shape. But to get a more precise conclusion on this issue, we should perform the simulation campaign mentioned above. It is interesting to notice that the kernel value we observe in our simulation are of the same order of magnitude of the term C in ST, that is, the term related to the collision between drops moving with the air. Therefore, the gravitational deposition that carries about 300,000 droplets, out of 10 million, outside the computational domain does not seem to have in the kernel statistics obtained from the simulation the same impact it has in the ST model.

In any case, the important clue we got from both the monodisperse and polydisperse population simulations is that the unsteady turbulence mixing confining the cloud region does not suppress the droplet collisional activity. In a time span where the kinetic energy of the air flow hosting the cloud is dropping of the 90%, the collision activity reduces by the 40% inside the cloud but rises by the 25% in the interaction mixing with the clear air. A result of the very rapid differentiation of the size of the droplets due to the different weight that evaporation and condensation have in the highly intermittent mixing region. A fact that could, at least in part, explain the rapid increase in the size of the droplets that is observed in some formations of cumulus clouds, in particular the maritime ones, and which is considered capable of inducing rainfall.

As an outlook, we would like to conduct a simulation campaign focusing on the micro-physics and dynamics present within the clouds and their border regions on larger domain scales than those here considered and with a sample size sufficient to obtain a good discretization of the collision-coalescence kernel capable to yield an analytical representation. To obtain a long observation window corresponding to one minute of the real phenomenon instead of the few

seconds of the present simulation, the background flow will be properly forced in different ways in the cloud and in the region of clean air. This is in order to keep the kinetic energy relationship between the two regions as constant as possible over time.

Furthermore, in the future, it would be opportune to include in this type of direct numerical turbulent simulations the effects of possible droplet fragmentation during collision and of the electromagnetic radiation present in the atmosphere. And, in perspective, to think about how to leave the Boussinesq hypothesis that is filtering out important physical aspects such as, e.g., the presence of acoustic-gravity waves in the atmosphere.

## 6. Acknowledgements

This project has received funding from the Marie-Sklodowska Curie Actions (MSCA ITN ETN COMPLETE) under the European Union's Horizon 2020 research and innovation programme. Grant agreement n°675675, <http://www.complete-h2020network.eu>.

We acknowledge the CINECA award HP10CA7H4X, under the ISCRA initiative, for the availability of high performance computing resources and support. Computational resources were also provided by HPC@POLITO, a project of Academic Computing within the Department of Control and Computer Engineering at the Politecnico di Torino (<https://hpc.polito.it>).

## References

Armenio, v., Fiorotto, v.. The importance of the forces acting on particles in turbulent flows. *Physics of Fluids* 2001;13:2437–2440.

Atkinson, B., Zhang, J.. Mesoscale shallow convection in the atmosphere. *Review of Geophysics* 1996;34:403–431. doi:[10.1029/96RG02623](https://doi.org/10.1029/96RG02623).

Ayala, O., Grabowski, W.W., Wang, L.P.. A hybrid approach for simulating turbulent collisions of hydrodynamically interacting particles. *Journal of Computational physics* 2007;225(1):51–73. doi:[10.1016/j.jcp.2006.11.016](https://doi.org/10.1016/j.jcp.2006.11.016).

Ayala, O., Parishani, H., Chen, L., Rosa, B., Wang, L.P.. Dns of hydrodynamically interacting droplets in turbulent clouds: Parallel implementation and scalability analysis using 2d domain decomposition. *Computer physics Communications* 2013;185(12):3269–3290. doi:[10.1016/j.cpc.2014.09.005](https://doi.org/10.1016/j.cpc.2014.09.005).

Ayala, O., Parishani, H., Chen, L., Rosa, B., Wang, L.P.. Dns of hydrodynamically interacting droplets in turbulent clouds: Parallel implementation and scalability analysis using 2d domain decomposition. *Computer physics Communications* 2014;185(12):3269–3290. doi:[10.1016/j.cpc.2014.09.005](https://doi.org/10.1016/j.cpc.2014.09.005).

Batchelor, G.K.. The theory of homogeneous turbulence. Cambridge University Press 1953;38:64–65.

Beard, K.V., Durkee, R.I., Ochs, H.T.. Coalescence efficiency measurements for minimally charged cloud drops. *Journal of the Atmospheric Sciences* 2002;59:233–243. doi:[10.1175/1520-0469\(2002\)059<0233:CEMFMC>2.0.CO;2](https://doi.org/10.1175/1520-0469(2002)059<0233:CEMFMC>2.0.CO;2).

Bergougnoux, L., Bouchet, G., Lopez, D., Guazzelli, E.. The motion of solid spherical particles falling in a cellular flow field at low stokes number. *Physics of Fluids* 2014;26.

Briggs, D.A., Ferziger, J.H., Koseff, J.R., Monismith, S.G.. Entrainment in a shear-free turbulent mixing layer. *Journal of Fluid Mechanics* 1996;310:215–241. doi:[10.1017/S0022112096001784](https://doi.org/10.1017/S0022112096001784).

Chandrakar, , Kant, K., Cantrell, , Will, , Chang, K., Ciochetto, D., Niedermeier, D., Ovchinnikov, M., Shaw, R., Yang, F.. Aerosol direct effect from turbulence-induced broadening of cloud-droplet size distributions. *Proceedings of the National Academy of Sciences* 2016;113(50):14243–14248. doi:[10.1073/pnas.1612686113](https://doi.org/10.1073/pnas.1612686113).

Chandrakar, K., Saito, I., Yang, F., Cantrell, W., Gotoh, T., Shaw, R.A.. Droplet size distributions in turbulent clouds: experimental evaluation of theoretical distributions. *Quarterly Journal of the Royal Meteorological Society* 2020;146:483–504.

East, T.W.R., Marshall, J.S.. Turbulence in clouds as a factor in precipitation. *Royal Meteorological Society* 1954;doi:<https://doi.org/10.1002/qj.49708034305>.

Eaton, J.K., Fessler, J.R.. Preferential concentration of particles by turbulence. *International Journal of Multiphase Flow* 1994;20:169–209.

Flossman, A.I., Hall, W.D., Pruppacher, H.R.. A theoretical study of the wet removal of atmospheric pollutants.1. the redistribution of aerosol particle scaptured through nucleation and impaction scavenging by growing cloud drops. *Journal of the Atmospheric Science* 1985;.

Franklin, C.N.. Collision rates of cloud droplets in turbulent flow. *Journal of the Atmospheric Sciences* 2005;62(7):2451–2466. doi:[10.1175/JAS3493.1](https://doi.org/10.1175/JAS3493.1).

Gao, Z., Liu, Y., Li, X., Lu, C.. Investigation of turbulent entrainment-mixing processes with a new particle-resolved direct numerical simulation model. *Journal of Geophysical Research: Atmospheres* 2018;123(4):2194–2214.

Gerashchenko, S., Good, G., Warhaft, Z.. Entrainment and mixing of water droplets across a shearless turbulent interface with and without gravitational effects. *Journal of fluid mechanics* 2011;668:293.

Ghan, S.J., Abdul-Razzak, H., Nenes, A., Ming, Y., Liu, X.H., Ovchinnikov, M., Shipway, B., Meskhidze, N., Xu, J., Shi, X.. Droplet nucleation: Physically based parameterizations and comparative evaluation. *Journal of Advances in Modeling Earth Systems* 2011;

Gilbert, B.. Diffusion mixing in grid turbulence without mean shear. *Journal of Fluid Mechanics* 1980;100:349–365. doi:[10.1017/S002211208000119X](https://doi.org/10.1017/S002211208000119X).

Good, G., Gerashchenko, S., Warhaft, Z.. Intermittency and inertial particle entrainment at a turbulent interface: the effect of the large-scale eddies. *Journal of fluid mechanics* 2012;694:371.

Gotoh, T., Suehiro, T., Saito, I.. Continuous growth of cloud droplets in cumulus cloud. *New Journal of Physics* 2016;18(4):043042. doi:<http://stacks.iop.org/1367-2630/18/i=4/a=043042>.

Gotzfried, P., Kumar, B., Shaw, R.A., Schumacher, J.. Droplet dynamics and fine-scale structure in a shearless turbulent mixing layer with phase changes. *Journal of Fluid Mechanics* 2017;814:452–483. doi:[10.1017/jfm.2017.23](https://doi.org/10.1017/jfm.2017.23).

Howell, W.. The growth of cloud drops in uniformly cooled air. *Journal of meteorology* 1949;.

Hudson, J.G., Da, X.. Volatility and size of cloud condensation nuclei. *Journal of Geophysics Research-Atmospheres* 1996;101:4435–4442.

Iovieno, M., Cavazzoni, C., Tordella, D.. A new technique for a parallel dealiased pseudospectral navier-stokes code. *Computer physics Communications* 2001;141(047101).

Iovieno, M., Di Savino, S., Gallana, L., Tordella, D.. Mixing of a passive scalar across a thin shearless layer: concentration of intermittency on the sides of the turbulent interface. *Journal of Turbulence* 2014;:311–334doi:[10.1080/14685248.2014.905393](https://doi.org/10.1080/14685248.2014.905393).

Ireland, P.J., Collins, L.R.. Direct numerical simulation of inertial particle entrainment in a shearless mixing layer. *Journal of fluid mechanics* 2012;704:301.

Jensen, J.B., Charlson, R.J.. On the efficiency of nucleation scavenging. *Journal of Advances in Modeling Earth Systems* 1984;.

Knaepen, B., Debly Quy, O., Carati, D.. Direct numerical simulation and large-eddy simulation of a shear-free mixing layer. *Journal of Fluid Mechanics* 2004;514:153–172. doi:[10.1017/S0022112004000035](https://doi.org/10.1017/S0022112004000035).

Kohler, H.. The nucleus in and the growth of hygroscopic droplets. *Trans Faraday Soc* 1936;32(32):1152–1161. doi:<https://pdfslide.net/documents/the-nucleus-in-and-the-growth-of-hygroscopic-droplets.html>.

Kostoglou, M., Karabelas, A.J.. Evaluation of zero order methods for simulating particle coagulation. *Journal of Collide and Interface Science* 1994;163:420–431. doi:[10.1006/jcis.1994.1121](https://doi.org/10.1006/jcis.1994.1121).

Kumar, B., Schumacher, J., Shaw, R.A.. Lagrangian mixing dynamics at the cloudy–clear air interface. *Journal of the Atmospheric Sciences* 2014;71(7):2564–2580. doi:[10.1175/JAS-D-13-0294.1](https://doi.org/10.1175/JAS-D-13-0294.1).

Lanotte, A.S., Seminara, A., Toschi, F.. Cloud droplet growth by condensation in homogeneous isotropic turbulence. *Journal of the Atmospheric Sciences* 2009;66(6):1685–1697. doi:[10.1175/2008JAS2864.1](https://doi.org/10.1175/2008JAS2864.1).

Liu, Y.G., Hallett, J.. On size distributions of cloud droplets growing by condensation: A new conceptual model. *Journal of Atmospheric Science* 1998;55:527–536.

Maxey, M.R.. The motion of small spherical particles in a cellular flow field. *Physics of Fluids* 1987;30(7):1915–1928. doi:[10.1063/1.866206](https://doi.org/10.1063/1.866206).

McGraw, R., Liu, Y.G.. Brownian drift-diffusion model for evolution of droplet size distributions in turbulent clouds. *Geophysical Research Letters* 2006;33:L03802.

Monteith, J., Unsworth, M.. *Principles of environmental physics*, 3rd edition. Academic Press 2008;:440.

Ovadnevaite, J., Zuend, A., Laaksonen, A., Sanchez, K.J., Roberts, G., Ceburnis, D., Decesari, S., Rinaldi, M., Hodas, N., Facchini, M.C., Seinfeld, J.H., O'Dowd, C.. Surface tension prevails over solute effect in organic-influenced cloud droplet activation. *Nature* 2017;546:637–641.

Petersen, A.J., Baker, L., Coletti, F.. Experimental study of inertial particles clustering and settling in homogeneous turbulence. *Journal of Fluid Mechanics* 2019;864:925–970. doi:[10.1017/jfm.2019.31](https://doi.org/10.1017/jfm.2019.31).

Pruppacher, H.R., Klett, J.D.. *Micro physics of Clouds and Precipitation*. Atmospheric and Oceanographic Sciences Library, 1997.

Reade, W.C., Collins, L.R.. Effect of preferential concentration on turbulent collision rates. *Physics of Fluid* 2000;12(10):2530–2540. doi:[10.1063/1.1288515](https://doi.org/10.1063/1.1288515).

Rogers, R.R., Yau, M.K.. *A short course in cloud physics*. Oxford; New York: Pergamon Press 1989;113:269–276.

Ruetsch, G.R., Maxey, M.R.. The evolution of small-scale structures in homogenous isotropic turbulence. *Physics of Fluid* 1993;4(12):2747–2760. doi:[10.1063/1.858333](https://doi.org/10.1063/1.858333).

Saffman, P.G., Turner, J.S.. On the collision of drops in turbulent clouds. *Journal of Fluid Mechanics* 1955;1:16–30. doi:<https://doi.org/10.1017/S0022112056000020>.

Saito, I., Gotoh, T.. Turbulence and cloud droplets in cumulus clouds. *New Journal of Physics* 2018;20(023001).

Saito, I., Gotoh, T., Watanabe, T.. Broadening of cloud droplet size distributions by condensation in turbulence. *Journal of the Meteorological Society of Japan* 2019;19:867–891.

Seinfeld, J.H., Pandis, S.N.. Atmospheric chemistry and physics from air pollution to climate change. *J Am Chem Soc* 1998;.

Siewert, C., Bec, J., Krstulovic, G.. Statistical steady state in turbulent droplet condensation. *Journal of Fluid Mechanics* 2017;810:254–280.

Tetens, O.. Tetens equation. *Über einige meteorologische Begriffe* 270Z *Geophys* 1930;6:207–309.

Teukolsky, S.A., Flannery, B.P., Press, W., Vetterling, W.. Numerical recipes in C. Cambridge University Press, 1992. URL: <https://doi.org/10.2307/3619708>.

Tordella, D., Iovieno, M.. Numerical experiments on the intermediate asymptotics of shear-free turbulent transport and diffusion. *Journal of Fluid Mechanics* 2006;549:429–441. doi:[10.1017/S0022112005007688](https://doi.org/10.1017/S0022112005007688).

Tordella, D., Iovieno, M.. Small scale anisotropy in turbulent shearless mixing. *Physical Review Letters* 2011;19(8):555–574.

Tordella, D., Iovieno, M.. Decaying turbulence: What happens when the correlation length varies spatially in two adjacent zones. *Physica D - Nonlinear Phenomena* 2012;241(3):178–185. doi:[10.1016/j.physd.2011.09.001](https://doi.org/10.1016/j.physd.2011.09.001).

Tordella, D., Iovieno, M., Bailey, P.R.. Sufficient condition for gaussian departure in turbulence. *Physical Review E* 2008;77(1):016–309. doi:[10.1103/PhysRevE.77.016309](https://doi.org/10.1103/PhysRevE.77.016309).

Vaillancourt, P.A., Yau, M.K., Bartello, P., Grabowski, W.W.. Microscopic approach to cloud droplet growth by condensation. part ii: Turbulence, clustering, and condensational growth. *Journal of the Atmospheric Sciences* 2002;59(24):3421–3435. doi:[10.1175/1520-0469\(2002\)059<3421:MATCDG>2.0.CO;2](https://doi.org/10.1175/1520-0469(2002)059<3421:MATCDG>2.0.CO;2).

Vaillancourt, P.A., Yau, M.K., Grabowski, W.W.. Microscopic approach to cloud droplet growth by condensation. part i: Model description and results without turbulence. *Journal of the Atmospheric Sciences* 2001;58(14):1945–1964. doi:[10.1175/1520-0469\(2001\)058<1945:MATCDG>2.0.CO;2](https://doi.org/10.1175/1520-0469(2001)058<1945:MATCDG>2.0.CO;2).

Vanni, M.. Approximate population balance equations for aggregation-breakage processes. *Journal of Collide and Interface Science* 1999;22(2):143–160. doi:[10.1006/jcis.1999.6571](https://doi.org/10.1006/jcis.1999.6571).

Veeravalli, S., Warhaft, Z.. The shearless turbulence mixing layer. *Journal of Fluid Mechanics* 1989;207:191–229. doi:[10.1017/S0022112089002557](https://doi.org/10.1017/S0022112089002557).

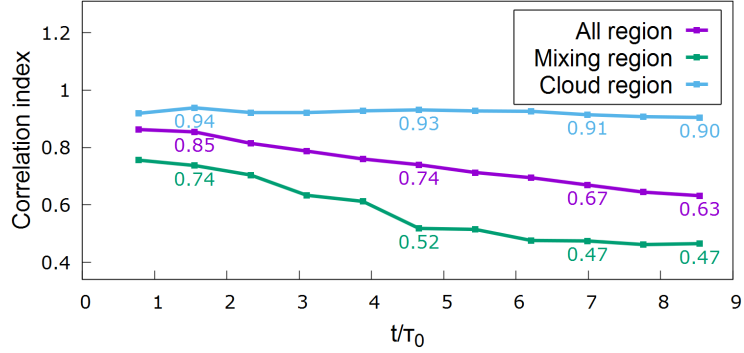
Wang, L.P., Wexler, A.S., Zhou, Y.. Statistical mechanical description and modelling of turbulent collision of inertial particles. *Journal of Fluid Mechanics* 2005;415:117–153.

Woods, J.D., J., M.B.. The wake capture of water drops in air. *Quarterly Journal of the Royal Meteorological Society* 1965;91:35–43. doi:<https://doi.org/10.1002/qj.49709138706>.

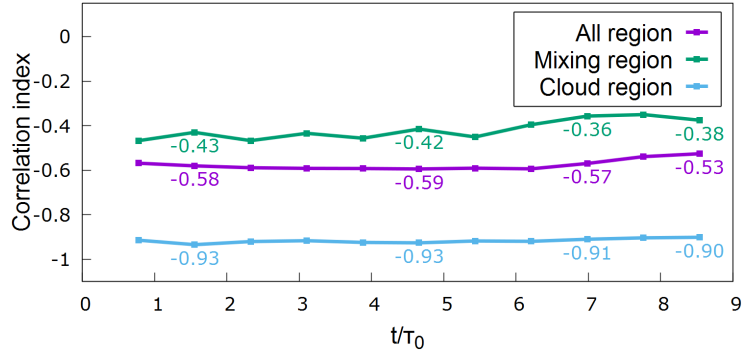
Wray, A.. Decaying isotropic turbulence. In AGARD Advisory Rep 1998;345:63–64.

Wu, W., McFarquhar, G.M.. Statistical theory on the functional form of cloud particle size distributions. *Journal of Atmospheric Science* 2018;75:2801–2814.

(a) Standard deviation of velocity longitudinal derivative and collision count



(b) Skewness of velocity longitudinal derivative and collision count



(c) Kurtosis of velocity longitudinal derivative and collision count

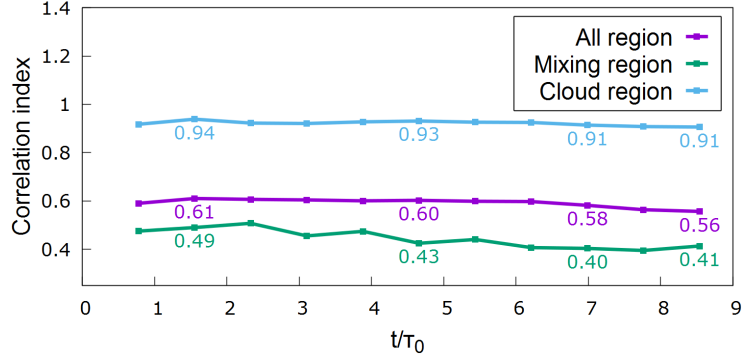


Figure 24: Correlation between the small scale dynamics of the turbulent velocity field and the droplet collision count. In particular, the correlation is between the intermittency of the velocity small scale fluctuation, showed via anisotropy related quantities, the skewness and the kurtosis of the longitudinal derivative fluctuation  $\partial u_3 / \partial x_3$ , see Tordella and Iovieno (2011), and the collision count.